



Title	Cyclic steps on ice
Author(s)	Yokokawa, M.; Izumi, N.; Naito, K.; Parker, G.; Yamada, T.; Greve, R.
Citation	Journal of Geophysical Research: Earth Surface, 121(5), 1023-1048 https://doi.org/10.1002/2015JF003736
Issue Date	2016-05-24
Doc URL	http://hdl.handle.net/2115/64599
Rights	Copyright 2016 American Geophysical Union. All Rights Reserved.
Type	article
File Information	Yokokawa_et_al-2016-Journal_of_Geophysical_Research__Earth_Surface.pdf



[Instructions for use](#)

RESEARCH ARTICLE

Cyclic steps on ice

10.1002/2015JF003736

Key Points:

- Cyclic steps on ice below flowing water form in an experimental flume
- A linear stability analysis provides a physical explanation of the formation of antidunes
- The experimental data fall in the region where the analysis predicts interfacial instability

Correspondence to:

M. Yokokawa,
miwa@is.oit.ac.jp

Citation:

Yokokawa, M., N. Izumi, K. Naito, G. Parker, T. Yamada, and R. Greve (2016), Cyclic steps on ice, *J. Geophys. Res. Earth Surf.*, 121, 1023–1048, doi:10.1002/2015JF003736.

Received 4 OCT 2015

Accepted 4 APR 2016

Accepted article online 7 APR 2016

Published online 24 MAY 2016

M. Yokokawa¹, N. Izumi², K. Naito³, G. Parker⁴, T. Yamada², and R. Greve⁵

¹Faculty of Information Science, Osaka Institute of Technology, Hirakata, Japan, ²Faculty of Engineering, Hokkaido University, Sapporo, Japan, ³Department of Civil and Environmental Engineering, University of Illinois, Urbana-Champaign, Illinois, USA, ⁴Department of Civil and Environmental Engineering, Department of Geology, University of Illinois at Urbana-Champaign, Urbana, Illinois, USA, ⁵Institute of Low Temperature Science, Hokkaido University, Sapporo, Japan

Abstract Boundary waves often form at the interface between ice and fluid flowing adjacent to it, such as ripples under river ice covers, and steps on the bed of supraglacial meltwater channels. They may also be formed by wind, such as the megadunes on the Antarctic ice sheet. Spiral troughs on the polar ice caps of Mars have been interpreted to be cyclic steps formed by katabatic wind blowing over ice. Cyclic steps are relatives of upstream-migrating antidunes. Cyclic step formation on ice is not only a mechanical but also a thermodynamic process. There have been very few studies on the formation of either cyclic steps or upstream-migrating antidunes on ice. In this study, we performed flume experiments to reproduce cyclic steps on ice by flowing water, and found that trains of steps form when the Froude number is larger than unity. The features of those steps allow them to be identified as ice-bed analogs of cyclic steps in alluvial and bedrock rivers. We performed a linear stability analysis and obtained a physical explanation of the formation of upstream-migrating antidunes, i.e., precursors of cyclic steps. We compared the results of experiments with the predictions of the analysis and found the observed steps fall in the range where the analysis predicts interfacial instability. We also found that short antidune-like undulations formed as a precursor to the appearance of well-defined steps. This fact suggests that such antidune-like undulations correspond to the instability predicted by the analysis and are precursors of cyclic steps.

1. Introduction

Boundary waves often form on the interface between ice and fluid flowing adjacent to it. One of the early studies on such boundary waves was performed by Carey [1966, 1967]. He observed ripples formed on the underside of ice that covers the water surface of some winter rivers, as shown in Figure 1a. Ice ripples are formed by the solidification of water when the water surface is cooled below freezing. An initially flat interface between ice and water flowing underneath it becomes unstable and evolves into a train of waves. Ashton and Kennedy [1972] have performed a simple linear stability analysis on the formation of ice ripples with the use of the Stefan condition and shown that a phase shift of heat flux contribution relative to the boundary waves can cause instability of initially flat boundaries. Gilpin *et al.* [1980] used a linear stability analysis to show that the boundary becomes unstable and that the resulting boundary waves migrate downstream if the relevant phase shift is in the range between $\pi/2$ and π . They have also conducted experiments with the use of a water tunnel and used them to validate the results of their analysis. Recently, Camporeale and Ridolfi [2012] have performed a detailed and complete linear stability analysis with minimal assumptions to explain the formation of ice ripples under free surface water flow. They showed that the ice-water interface can be unstable even in the case of laminar flow, so that the instability is not particular to turbulent flow. Related stability analyses pertaining to ice and karst (calcite) morphodynamics can be found in Vesipa *et al.* [2015] and Camporeale [2015].

Another example of boundary waves formed on an ice surface is a series of steps observed on a relatively steep bed surface of a supraglacial meltwater stream (Figure 1b). Again, the initially flat ice surface of the meltwater stream bed becomes unstable, so that the ice-water interface becomes covered with a series of steps, each of which is delineated by hydraulic jumps upstream and downstream. Similar cyclic steps on ice may be formed by not only flowing water but also by wind. Troughs sculpted in a spiral shape can be observed on the polar ice caps of Mars (Figure 1c). Though the formation process of these spiral troughs is not yet completely understood, Smith *et al.* [2013] have suggested that the spiral troughs are likely cyclic steps formed

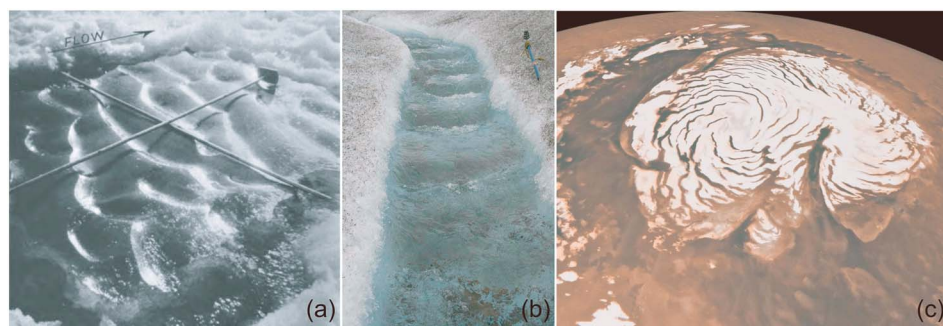


Figure 1. (a) Ice ripples formed on the underside of the ice that covers the water surface of a river (from Carey [1966]). (b) Ice steps formed in a channel on the surface of glacier ice (courtesy L. Karlstrom). (c) Spiral troughs on Mars North Polar Ice Cap (courtesy NASA/JPL-Caltech).

by katabatic wind blowing over the ice caps. A katabatic wind is a gravity flow of air accelerated by the process by which the air is cooled from underneath by ice. The formation of cyclic steps on the ice surface would be associated with the uneven solidification or sublimation of water vapor contained in the katabatic wind. According to Smith *et al.* [2013], sublimation is enhanced in the steep portion where the katabatic wind accelerates toward a hydraulic jump, while deposition of frost causes solidification at the site of the hydraulic jump. There is a strong downward airflow right at the Martian poles. This downward atmospheric flow reaches the surface of Mars and changes flow direction so as to be parallel to the surface and directed radially away from the pole. This radial flow takes a spiral path due to the Coriolis force. Cyclic steps are formed subperpendicularly to the wind direction, so that the steps are in a spiral shape as well. Similar bedforms (megadunes) have been discovered on the Antarctic ice sheet on the Earth [Fahnestock *et al.*, 2000; Frezzotti *et al.*, 2002]. Some of these might be cyclic steps formed by a katabatic wind flowing over the surface of Antarctica.

Cyclic steps are spatially periodic bedforms observed on relatively steep slopes. Each step is delineated by upstream and downstream hydraulic jumps in the flow above the bed. They tend to migrate upstream, keeping an almost constant wavelength. Recently cyclic steps have been reported from various environments on the Earth, such as fluvial and deep-sea settings, and in various bed materials, such as bedrock, noncohesive sediment and cohesive sediment [e.g., Kostic *et al.*, 2010]. There have been some theoretical and experimental work aimed at revealing the formative conditions and detailed features of cyclic steps [e.g., Parker and Izumi, 2000; Brooks, 2001; Taki and Parker, 2005; Yokokawa *et al.*, 2009, 2011; Izumi *et al.*, 2012; Cartigny *et al.*, 2014].

While the formation of cyclic steps on bedrock or a bed composed of sediment is a mechanical process associated with differential transport of sediment, the formation of cyclic steps on ice is not only a mechanical but also a thermodynamic process. To the authors' knowledge, there have been very few studies on the thermodynamics of the formation of cyclic steps on ice. In this study, we conducted a series of experiments on the formation of cyclic steps at the interface between ice and flowing water above. In addition, we performed a linear stability analysis of the water-ice interface similar to Camporeale and Ridolfi [2012]. As explained below, cyclic steps themselves are a fundamentally nonlinear phenomenon and cannot be explained in terms of linear stability analysis. A precursor form consisting of upstream-migrating antidunes can, however, be so explained. We show here that the formation of cyclic steps can be explained in part by the results of our analysis.

2. Experiments

2.1. Experimental Setup

2.1.1. Experimental Apparatus

The experiments were conducted in the cold chamber of the Institute of Low Temperature Science (ILTS), Hokkaido University. This cold chamber can be cooled to a temperature down to -20°C . We conducted eight cases of experiments by the use of an experimental apparatus set in the cold chamber, consisting of a flume, a cooling system for the flume, and a circulating system for water, as shown in Figure 2.

The flume is made of Plexiglas and is 180 cm long, 4 cm wide, and 20 cm deep. It has two weirs 30 cm downstream from the upstream end and located right at the downstream end of the flume itself. Water is stored and frozen between these two weirs to make a 150 cm long and 8 cm deep ice floor at the bottom of

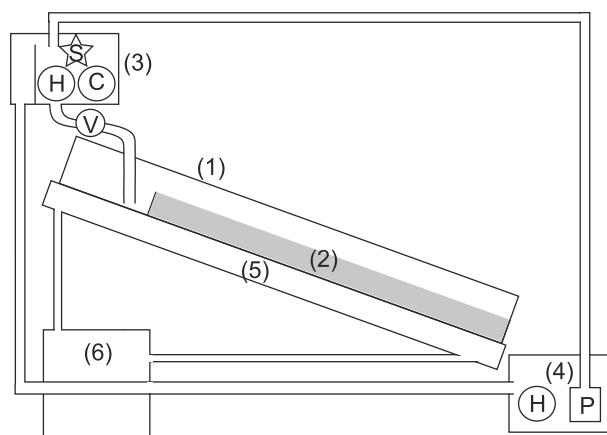


Figure 2. A conceptual diagram of the experimental apparatus. (1) Flume, (2) ice bed, (3) upper tank, (4) lower tank, (5) cooling tank of the flume, and (6) low constant temperature circulating bath. P: pump, H: heater, C: cooling tank, V: Valve, and S: stirrer.

the flume. In addition, the flume width can be adjusted by installing several thin Plexiglas plates, each with a length of 150 cm, width of 20 cm, and thickness of 5 mm. According to *Camporeale and Ridolfi* [2012], Squire's theorem does not apply in the case of ice bed instability. Therefore, the flat ice surface is more unstable for three-dimensional perturbations than two-dimensional ones. In order to constrain three-dimensional perturbations, we reduced the flume width to be 2 cm or 1 cm, respectively, by installing either four or six plates into the flume. A minor discrepancy between the analysis and the experiments arises in that sidewall effects are not included in the two-dimensional stability analysis.

The cooling system of the flume is a tank made of vinyl chloride, the length,

width, and height of which are 184 cm, 16 cm, and 5 cm, respectively. A refrigerant liquid, ethyl alcohol cooled down to around -17°C , was circulated in the tank with a low constant temperature circulating bath (As One LTB-400). We placed the whole flume, including the ice, upon the cooling tank so as to cool the ice from the bottom.

The circulating system of water is composed of upper and lower tanks, as well as a pump installed in the lower tank in order to pump up water from the lower to upper tank. Water flows from the upper tank to the flume. The discharge of water is controlled with a valve installed on the hose between the upper tank and the flume. Water from the upper tank first flows into a reservoir upstream of the upstream-most weir in the flume. It then overflows the weir and flows on the ice surface. Finally, water flows into the lower tank, and is pumped back up into the upper tank. In order to keep the water temperature at a target temperature (0.1 to 0.4°C in this study), we installed an immersion type cooler (Yamato Scientific Co., Ltd., Neocool Dip BE200F) and an immersion type heater with a thermostat (Yamato Scientific Co., Ltd., Thermomate BF200) into the upper tank. In addition, we dyed the water with a green food coloring agent to distinguish water from ice.

2.1.2. Temperature Settings

One of the purposes of our experiments was to study the morphological evolution of the ice surface through melting and freezing due to temperature differences among ice, flowing water, and the surrounding air. Therefore, it is of great importance to control their temperatures. In the formation process of ice steps on glaciers, the temperature of flowing water is higher than that of the ice and lower than the surrounding air temperature. In the formation process of spiral troughs on Mars, however, the flowing fluid is not water but mostly carbon dioxide including water vapor. It is further suspected that the temperature of flowing gas is higher than the ice temperature and lower than the ambient air temperature [e.g., *Smith et al.*, 2013]. Keeping these factors in mind, we kept the ice temperature below 0°C , the water temperature in the range 0.2 to 2°C , and the room temperature at about 5°C .

2.1.3. Measurements

To measure the water discharge, we collected water discharged from the downstream end of the flume in a beaker for several to several tens of seconds. Then we calculated the discharge by dividing the amount of water in the beaker by the sampling time. The flow depth was measured by a scale marked in 10 cm intervals during the period when no bedforms had yet appeared, i.e., shortly after each run started. We took an average of the measured flow depths and used this average to define the initial flow depth on the flat bed. This value was used for the subsequent analyses.

The room temperature, water temperature (in the upper tank, the upstream reservoir, and the lower tank), and the upper surface temperature of the cooling tank (the bottom surface temperature of the flume) were continuously measured by the use of temperature probes and wireless data loggers. In addition, the inside temperature of the ice was monitored by temperature probes, each of which was 0.1 mm in diameter, installed

Table 1. Experimental Conditions^a

Run Number	Channel Width (cm)	Channel Slope (deg)	Room Temp. (°C)	Water Temp. (°C)	Ice Temp. (°C)	Discharge (cm ³ /s)	Initial Flow Depth (mm)	Froude Num.
CSIM120908A	2	5	5.5	0.7	−1.85	8.83	2.05	1.52
CSIM120910A	2	5	9.3	1.9	−1.66	8.36	1.45	2.42
CSIM120910B	2	5	5.7	0.7	−1.62	13.29	1.65	3.17
CSIM120911A	1	20	5.5	0.5	−1.62	13.16	2.12	4.31
CSIM120911B	2	5	5.2	0.2	−1.69	77.9	5.7	2.89
CSIM120912A	2	0.9	5.4	0.5	−2.02	11.7	4.14	0.702
CSIM120913A	2	5	5.3	2.2	−2.86	7.6	2.29	1.11
CSIM120914A	2	20	5.4	0.5	−1.77	12.1	1.25	4.37

^aThe ice temperatures were measured 2 cm above the three locations and averaged for 1 h before each experiment finished.

in the ice. The temperature probes inside the ice were set at eight locations: 2 cm, 4.5 cm, and 7 cm above the ice bottom at 30 cm downstream from the upstream weir, 2 cm and 4.5 cm above the ice bottom at 85 cm downstream from the upstream weir, and 2 cm, 4.5 cm, and 7 cm above the ice bottom at 140 cm downstream from the upstream weir.

The topography of the ice surface was measured with the use of photographs taken every one minute during the experiments.

2.2. Experimental Results

2.2.1. Outline of Experimental Results

We performed eight experiments in the settings described in section 2.1. The room temperature \bar{T}_a was set to be around 5°C, except one case when the average room temperature kept at 9.3°C. The water temperature \bar{T}_f ranged from 0.2 to 2.2°C, and the ice bottom temperature \bar{T}_b ranged from −2.86 to −1.62°C. The channel slope angle θ was set to be 0.9, 5, and 20°, and the flow discharge was set between 7.60 and 77.90 cm³/s. The flow depths \bar{H}_0 on the initial flat bed were found to range between 1.25 and 5.70 mm.

Two key dimensionless parameters governing the flow are the Froude Number Fr and the Reynolds Number Re . These parameters can be defined as follows:

$$Fr = \frac{\bar{U}_a}{\sqrt{g\bar{H}_0}}, \quad (1)$$

$$Re = \frac{\bar{U}_a\bar{H}_0}{\nu}, \quad (2)$$

where \bar{U}_a is the depth-averaged velocity, g is the gravitational acceleration ($= 9.8 \text{ m/s}^2$), and ν is the kinematic viscosity. In our experiments the Froude number was found to range from 0.70 to 4.37. Except for one case, the Reynolds numbers were smaller than 750, so the flow can be assumed to be laminar or transitional [Lajeunesse *et al.*, 2010; Camporeale and Ridolfi, 2012]. Weak roll waves were observed in all cases. We ran each experiment for approximately 4 h. A summary of the experimental conditions is shown in Table 1.

We made ice for the experimental flume in another room with a temperature of −20°C at the ILTS before we started each experiment. We placed the flume with ice on the cooling tank and began supplying water from the upper tank to the flume. Therefore, the temperature of the whole channel was initially around −15°C. The temperature of the ice subsequently increased due to the relatively high room temperature and approached an equilibrium temperature after about 2 h. One example of the time variation of ice temperature is shown in Figure 3. We observed the formation of step-like bedforms (referred to as steps hereafter) in the cases for which the Froude number was larger than unity, while no bedforms were observed to have formed in the single case for which the Froude number was subcritical, with a value of 0.70. In most of the cases in which steps eventually formed, significant growth of bedforms was observed after the equilibrium temperature was achieved. A summary of the experimental results is shown in Table 2.

2.2.2. Morphology of Steps

We measured the wavelength \bar{L} and wave height $\bar{\eta}$ of steps in the photographs taken at the end of each experiment (Table 2). Here the wavelength \bar{L} is defined as the distance from one step to the adjacent step measured

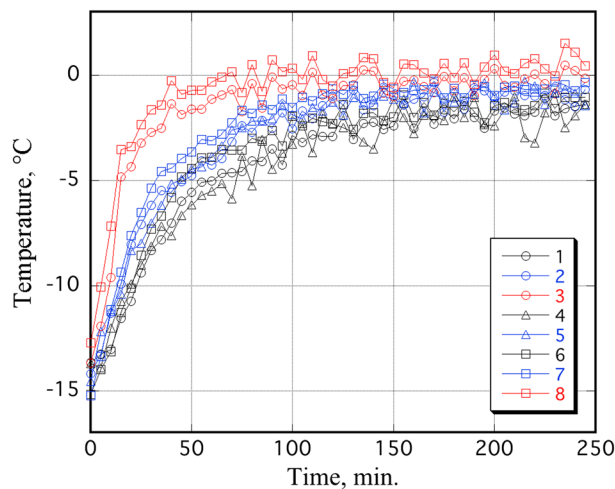


Figure 3. An example of the time variation of ice temperature (CSIM120911B). The ice temperature is -15°C at the beginning but reaches an equilibrium temperature after about 2 h. The temperature is measured at (1) 2 cm, (2) 4.5 cm, and (3) 7 cm above the ice bottom 30 cm downstream from the upstream weir, (4) 2 cm and (5) 4.5 cm above the ice bottom 85 cm downstream from the upstream weir, (6) 2 cm, (7) 4.5 cm, and (8) 7 cm above the ice bottom 140 cm downstream from the upstream weir.

streamwise along the general trend of the bed slope, and the wave height as the distance between the highest point of a crest and the lowest point of the trough immediately downstream, measured orthogonal to the bed. We took an algebraic average of data for each experimental case. The average wavelengths were determined to range from 34.3 cm and 125 cm, while the wave heights ranged from 1.62 to 4.62 cm. It follows that the wave steepness (wave height/wavelength) was in the range 0.018 to 0.177.

In Figure 4, the average wavelengths are plotted against the initial flow depth \tilde{H}_0 for the flat bed. It is found from the figure that the average wavelength increases with increasing flow depth (see also Figure 5). The nondimensional wave number α , given as

$$\alpha = \frac{2\pi\tilde{H}_0}{\tilde{L}} \quad (3)$$

is plotted against the Froude number in Figure 6. We can see a tendency for the nondimensional wave number to be almost constant, independent of the Froude number.

Note that, in general, the flow upstream of the depression associated with each step is shallow, while the flow downstream of the depression is deep, as shown in Figure 7. This implies that water flows down the upstream shallow part of the depression as supercritical flow in the Froude sense, and flows in the downstream deeper region as subcritical flow. A submerged hydraulic jump [Rajaratnam, 1967] takes place between the upstream shallow region and the downstream deeper region.

2.2.3. Development Processes of Steps

In the case for which the ice surface was rather flat and any initial disturbances on the bed, such as cavities or cracks on the ice surface, were minimal, a step first formed at the downstream end of the channel due to the effect of the downstream end (see Figure 8, (2)). As the step at the downstream end grew, another step started to grow some distance farther upstream (see Figure 8, (3) and (4)). Subsequently as those steps grew, another step farther upstream started to grow (see Figure 8, (5) and (6)). When the ice surface initially possessed noticeable cavities or cracks, these triggered local melting of the ice surface. In these cases, steps did not necessarily form from the downstream end. However, a second step still tended to form some distance upstream of the first one. Regardless of triggering mechanism, we suggest that the wavelength of steps should be self-selected depending on hydraulic conditions.

Table 2. Experimental Results

Run Number	Reynolds Number	Wavelength		Wave steepness	T_b	B
		(m)	Wave number			
CSIM120908A	252	0.45	0.0286	0.071	0.34	29
CSIM120910A	249	0.575	0.0158	0.028	0.18	41
CSIM120910B	380	0.365	0.0284	0.08	0.28	36
CSIM120911A	747	0.45	0.0296	0.089	0.29	28
CSIM120911B	2190	1.25	0.0287	0.018		
CSIM120912A	332	NA	NA	NA	0.37	14
CSIM120913A	228	0.473	0.0304	0.078	0.54	26
CSIM120914A	343	0.343	0.0229	0.177	0.33	48

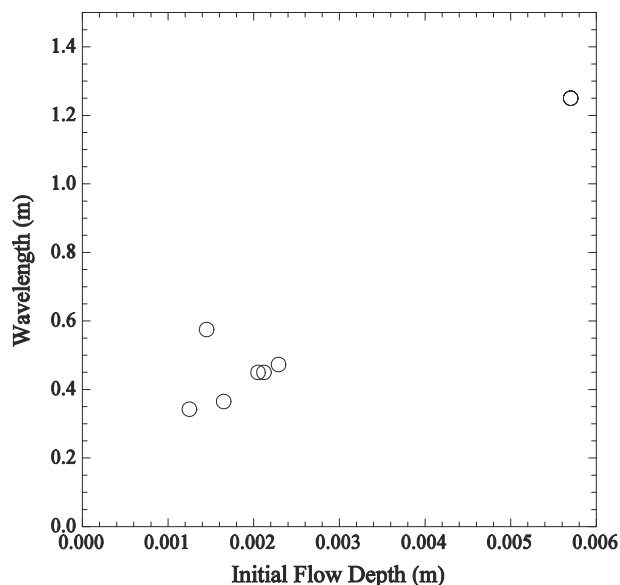


Figure 4. Wavelength of steps versus initial flow depth.

2.3. Comparison of the Morphology of the Ice Steps With Upper Flow Regime Bedforms on Alluvial Sand Beds

There are a limited number of experimental studies of wavy structures on ice surfaces, and most of them are studies of “ripples” in a closed channel configuration [e.g., Ashton and Kennedy, 1972; Fuhs et al., 1980]. There appears to have been no experimental study on the behavior of ice-water interfaces under Froude-supercritical open channel flow conditions, and indeed there are no systematic definitions for those bedforms. With this in mind, we compare the geometry of these wavy structures on an ice surface with corresponding bedforms formed on sand beds by Froude-supercritical flow. The morphology on the ice surface is formed by the trade-off of heat flux between the ice and the fluid, whereas the morphology of the sand surface is formed by the differential transport of sediment by flow. At this moment, we do not have any information as to how to directly compare those two kinds of morphologies. Although further discussion is required, here we assume that the geometry of the surface morphology reflects some hydraulic conditions common to ice beds

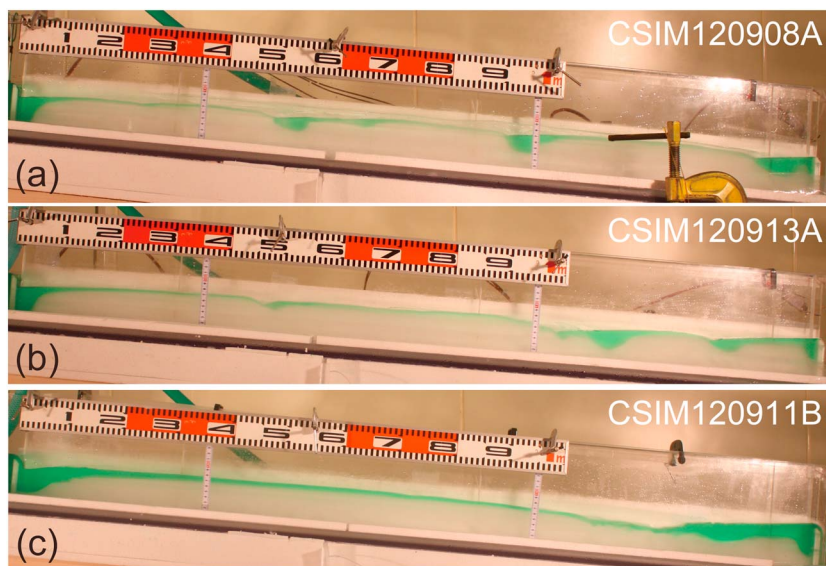


Figure 5. Examples of steps formed in the experiments. Run number, initial flow depth, and average wavelength (see Tables 1 and 2) are (a) CSIM120908A, 2.05 mm, 45 cm, (b) CSIM120913A, 2.29 mm, 47.3 cm, and (c) CSIM120911B, 5.70 mm, 125 cm, respectively.

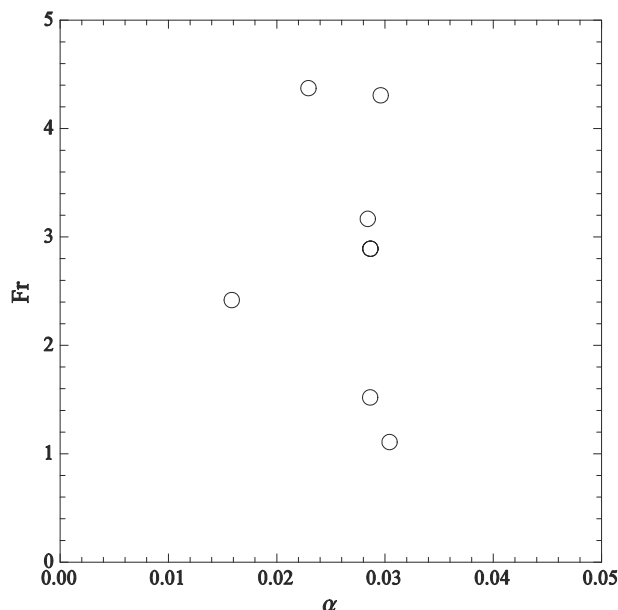


Figure 6. Froude number versus wave number of the steps.

and alluvial beds. Here we employ two dimensionless parameters to characterize the data, i.e., wave steepness $\tilde{\eta}/\bar{L}$ and nondimensional wave number, $\alpha = 2\pi\tilde{H}_0/\bar{L}$. Both these parameters have been very commonly used to describe bedforms [e.g., van Rijn, 1984; Julien and Klaassen, 1995].

Fukuoka *et al.*'s study [1982] is one of the earliest of the relatively few experimental studies which describe the complete range of upper flow regime bedforms on sand beds in open channels, including upstream-migrating antidunes, downstream-migrating antidunes, and chute-and-pool bedforms (cyclic steps) in a single treatment. They found that the wave steepness for dunes, upstream-migrating antidunes and downstream-migrating antidunes are about 0.02, 0.01, and 0.05–0.1, respectively. We also calculated the nondimensional wave number using their data sets to express the relationship between the wavelength and the flow depth. The wave number of upstream-migrating antidunes and downstream-migrating antidunes ranges from 0.24 to 0.41 and from 0.82 to 1.99, respectively (Figure 9). Taki and Parker [2005] summarize experiments on transportational cyclic steps in alluvium. Using their data sets, we calculated the wave steepness for their cyclic steps; it was found to range from 0.02 to 0.09, with the nondimensional wave number ranging from 0.01 to 0.03. Subsequently, Yokokawa *et al.* [2011] described the features of a variety of bedforms formed in upper regime flow, such as upstream-migrating antidunes, downstream-migrating antidunes, cyclic steps, and bedforms that show features that are transitional between antidunes and cyclic steps. They focused on the differences in hydraulic conditions and morphologic features of bed and water surface waves associated with cyclic steps and antidunes. That is, cyclic steps maintain their bounding by hydraulic jumps, while antidunes do not necessarily do so. In addition water surface waves break periodically for some types of antidunes,

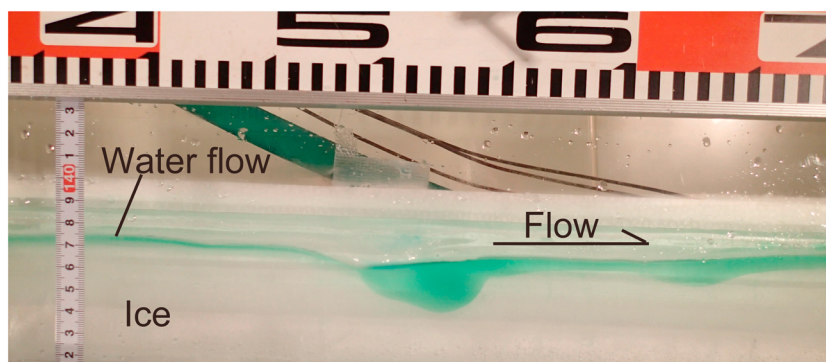


Figure 7. Depression formed just downstream of a step. Flow is left to right. Run number CSIM120908A.

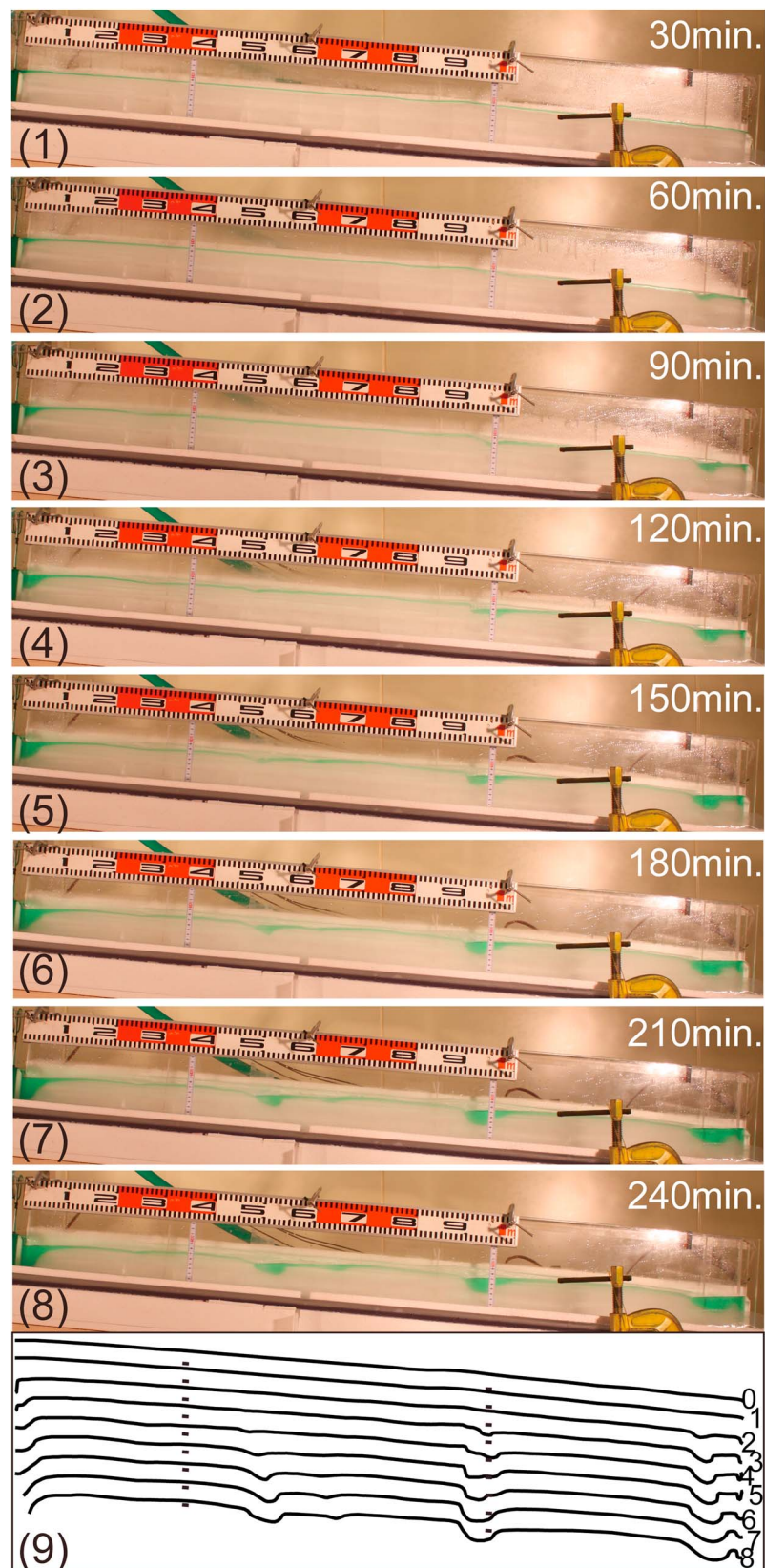


Figure 8. Development process of steps. (Run number CSIM120908A). (1) 30 min, (2) 60 min, (3) 90 min, (4) 120 min, (5) 150 min, (6) 180 min, (7) 210 min, (8) 234 min subsequent to run initiation. Flow is left to right. (9) Line drawings of ice surface for every 30 min correspondent to (1)–(8).

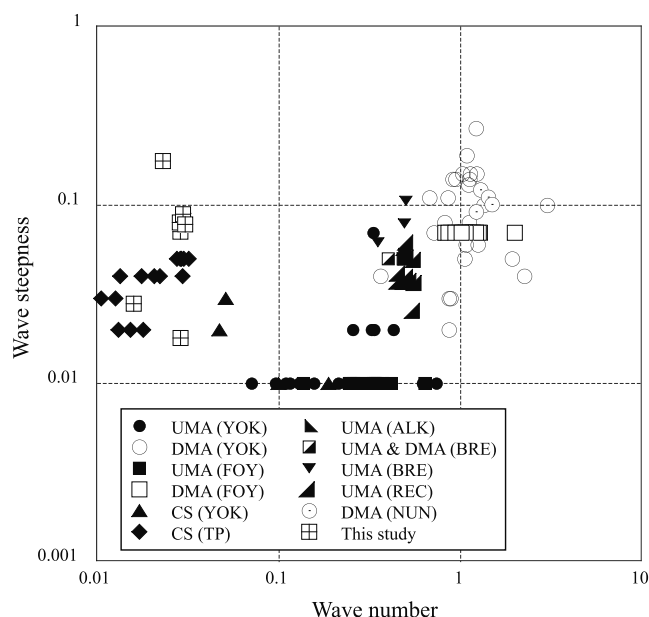


Figure 9. Wave steepness and wave numbers for antidunes, cyclic steps, and ice waves. YOK: Yokokawa *et al.* [2011], FOY: Fukuoka *et al.* [1982], TP: Taki and Parker [2005], ALK: Alexander *et al.* [2001], BRE: Bregoli [2008], REC: Recking *et al.* [2009], and NUN: Núñez-González and Martín-Vide [2011].

whereas they remain quite stable without breaking for other types. Yokokawa *et al.* also pointed out that the wavelength of downstream-migrating antidunes tends to be short compared to those of upstream-migrating antidunes. In Figure 9, we have also plotted data for antidunes from Alexander *et al.* [2001], Bregoli [2008], Recking *et al.* [2009], and Núñez-González and Martín-Vide [2011]. In the cases of Bregoli [2008] and Recking *et al.* [2009], the bed material was relatively coarse (with sediment median sizes of 7.34 mm for Bregoli [2008] and 2.3, 9.0, and 23.0 mm for Recking *et al.* [2009]). Their data show higher values of wave steepness compared with those for fine- to medium-grained sand.

The shape of the steps that we observed in our experiments using ice was characterized by long wavelength compared with the flow depth and relatively high wave height. Hence, the wave steepness and the nondimensional wave number ranged from 0.018 to 0.177 and from 0.015 to 0.031, respectively. These values fall into the region of cyclic steps on sand beds (Figure 9). Based on these geometric features and the upstream-expanding behavior noted above (see section 2.2.3) associated with hydraulic jumps (see section 2.2.2), the steps on ice observed in our experiments can be classified as analogous to cyclic steps formed on open channel sand beds.

3. Theoretical Analysis

3.1. Basis for the Analysis

Here we apply linear stability analysis to an open channel flow over ice with a wavy perturbation of infinitesimal amplitude at the water-ice interface. The goal is to study whether or not the flow is unstable to perturbations under conditions analogous to those observed experimentally herein, e.g., Froude-supercritical flow. The analysis presented here cannot be thought of as a direct stability analysis of cyclic steps themselves. This is because one of the defining factors of cyclic steps is the bounding of each step by hydraulic jumps. The discontinuity at each hydraulic jump precludes Taylor expansion around a steady, uniform base state; there is thus no such thing as a train of infinitesimal-amplitude cyclic steps.

Instead, what the analysis provides is a water-ice analog to the antidune instability. As explained in Parker and Izumi [2000], cyclic steps are closely tied to antidunes. The major discriminating factors between the two are (a) the existence of bounding hydraulic jumps in the case of cyclic steps and (b) the condition that cyclic steps are usually long-wave phenomena relative to depth, i.e., $\alpha \ll 1$, whereas antidunes are usually short-wave phenomena relative to depth, i.e., $\alpha \rightarrow o(1)$. Evidently antidunes can, in some cases, evolve to cyclic steps via nonlinear interaction between the flow and the bed. We expect, however, that an ice bed that is subject to the formation of cyclic steps should also display an analog of the antidune instability.

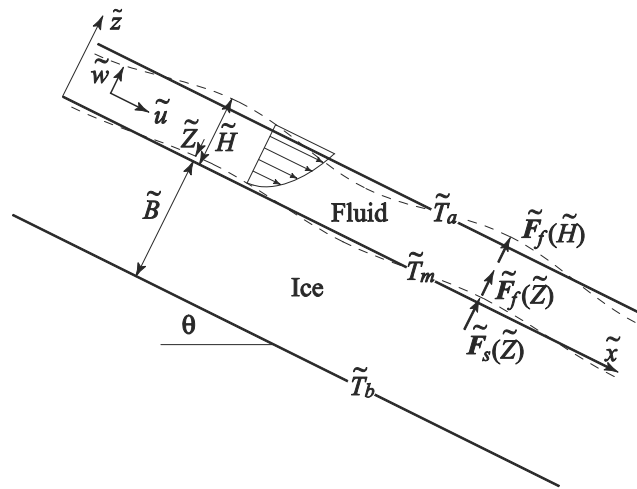


Figure 10. Conceptual diagram of flow and coordinates.

The linear stability analysis presented here is essentially the same as that of *Camporeale and Ridolfi* [2012], but some approximations and modifications are made in order to apply their work to our experimental results. First of all, we neglect the effect of surface tension because we focus on waves with sufficiently large wavelengths. Second, while *Camporeale and Ridolfi* [2012] assumed a completely equilibrium state as a base state for the stability analysis, the ice surfaces in our experiments are not necessarily in perfect equilibrium. Therefore, we employ the “frozen-time approximation” in which the ice surface corresponding to the base state of a stability analysis is time dependent, but the time variation is assumed to be negligible. Finally, we propose an alternative choice of the boundary condition for the heat transfer at the water surface in the analysis which is physically more realistic for the actual phenomena we study. The latter two issues are further discussed subsequently.

3.2. Flow Equations

Considering that, in most of the experimental cases studied here, the Reynolds number is smaller than 750, we assume that flow is laminar in our analysis [*Lajeunesse et al.*, 2010; *Camporeale and Ridolfi*, 2012]. In addition, we employ the quasi-steady assumption according to which the adjustment of flow and temperature takes place immediately, and therefore, the unsteady terms in the flow and heat transfer equations can be neglected.

The flow configuration shown in Figure 10 is described by the Navier-Stokes equations and the continuity equation, written in the forms

$$(\tilde{\mathbf{u}} \cdot \tilde{\nabla}) \tilde{\mathbf{u}} = -\frac{1}{\rho} \tilde{\nabla} \tilde{p} + \nu \tilde{\nabla}^2 \tilde{\mathbf{u}} + \tilde{\mathbf{g}} \tag{4}$$

$$\tilde{\nabla} \cdot \tilde{\mathbf{u}} = 0, \tag{5}$$

where $\tilde{\nabla}$ is the two-dimensional nabla operator, $\tilde{\mathbf{u}}$ is the velocity vector ($= (\tilde{u}, \tilde{w})$), \tilde{p} is the pressure, ρ is the density of water, and $\tilde{\mathbf{g}}$ is the gravitational acceleration vector. In this paper, the tildes indicate dimensional variables that will later be represented in dimensionless form with the tildes removed. The two-dimensional nabla operator $\tilde{\nabla}$ is defined by

$$\tilde{\nabla} = \left(\frac{\partial}{\partial \tilde{x}}, \frac{\partial}{\partial \tilde{z}} \right), \tag{6}$$

where \tilde{x} and \tilde{z} are the coordinates in the streamwise and upward normal directions, respectively. With the use of the slope angle θ , the gravitational acceleration vector $\tilde{\mathbf{g}}$ takes the form

$$\tilde{\mathbf{g}} = (g \sin \theta, -g \cos \theta). \tag{7}$$

The boundary conditions for the flow at the water surface are the kinematic boundary condition such that the flow component normal to the water surface vanishes, and the dynamic boundary conditions that the stresses normal and tangential to the water surface both vanish, i.e.,

$$\left. \begin{aligned} \tilde{\mathbf{u}} \cdot \tilde{\mathbf{e}}_{ns} &= 0 \\ \tilde{\mathbf{e}}_{ts} \cdot \tilde{\mathbf{T}} \cdot \tilde{\mathbf{e}}_{ns} &= 0 \\ \tilde{\mathbf{e}}_{ns} \cdot \tilde{\mathbf{T}} \cdot \tilde{\mathbf{e}}_{ns} &= 0 \end{aligned} \right\} \text{ at } \tilde{z} = \tilde{Z} + \tilde{H}, \quad (8)$$

where \tilde{Z} is the ice surface elevation and \tilde{H} is the flow depth. The stress tensor $\tilde{\mathbf{T}}$ is defined as

$$\tilde{\mathbf{T}} = \begin{bmatrix} \tilde{\tau}_{xx} & \tilde{\tau}_{xz} \\ \tilde{\tau}_{xz} & \tilde{\tau}_{zz} \end{bmatrix} \quad (9)$$

$$\tilde{\tau}_{xx} = -\tilde{p} + 2\rho\nu \frac{\partial \tilde{u}}{\partial \tilde{x}}, \quad (10)$$

$$\tilde{\tau}_{xz} = \rho\nu \left(\frac{\partial \tilde{u}}{\partial \tilde{z}} + \frac{\partial \tilde{w}}{\partial \tilde{x}} \right), \quad (11)$$

$$\tilde{\tau}_{zz} = -\tilde{p} + 2\rho\nu \frac{\partial \tilde{w}}{\partial \tilde{z}}, \quad (12)$$

with $\tilde{\mathbf{e}}_{ts}$ and $\tilde{\mathbf{e}}_{ns}$ denoting the unit vectors tangential and normal to the water surface, respectively, defined as

$$\tilde{\mathbf{e}}_{ts} = \frac{(1, \partial(\tilde{Z} + \tilde{H})/\partial \tilde{x})}{\left[1 + (\partial(\tilde{Z} + \tilde{H})/\partial \tilde{x})^2\right]^{1/2}}, \quad (13)$$

$$\tilde{\mathbf{e}}_{ns} = \frac{(-\partial(\tilde{Z} + \tilde{H})/\partial \tilde{x}, 1)}{\left[1 + (\partial(\tilde{Z} + \tilde{H})/\partial \tilde{x})^2\right]^{1/2}}. \quad (14)$$

At the bottom of the flowing water (i.e., the ice surface), the velocity components in the direction tangential and normal to the ice surface both vanish. These conditions take the forms

$$\left. \begin{aligned} \tilde{\mathbf{u}} \cdot \tilde{\mathbf{e}}_{tb} &= 0 \\ \tilde{\mathbf{u}} \cdot \tilde{\mathbf{e}}_{nb} &= 0 \end{aligned} \right\} \text{ at } \tilde{z} = \tilde{Z}, \quad (15)$$

where $\tilde{\mathbf{e}}_{tb}$ and $\tilde{\mathbf{e}}_{nb}$ are the unit vectors tangential and normal to the ice surface, respectively. The unit vectors $\tilde{\mathbf{e}}_{tb}$ and $\tilde{\mathbf{e}}_{nb}$ are defined as

$$\tilde{\mathbf{e}}_{tb} = \frac{(1, \partial \tilde{Z}/\partial \tilde{x})}{\left[1 + (\partial \tilde{Z}/\partial \tilde{x})^2\right]^{1/2}}, \quad (16)$$

$$\tilde{\mathbf{e}}_{nb} = \frac{(-\partial \tilde{Z}/\partial \tilde{x}, 1)}{\left[1 + (\partial \tilde{Z}/\partial \tilde{x})^2\right]^{1/2}}. \quad (17)$$

3.3. Heat Transfer Equations of Water and Ice and Stefan Condition

Applying the quasi-steady assumption, the heat transfer equation in flowing water takes the form

$$\rho c_v (\tilde{\mathbf{u}} \cdot \nabla) \tilde{T}_f + \nabla \cdot \tilde{\mathbf{F}}_f = 0, \quad (18)$$

where c_v is the specific heat of water and \tilde{T}_f is the temperature of water. In the above equation, $\tilde{\mathbf{F}}_f$ is the heat flux in water, described by

$$\tilde{\mathbf{F}}_f = \left(-k_f \frac{\partial \tilde{T}_f}{\partial \tilde{x}}, -k_f \frac{\partial \tilde{T}_f}{\partial \tilde{z}} \right), \quad (19)$$

where k_f is the heat conductivity of water.

The heat transfer equation in ice is

$$\tilde{\nabla} \cdot \tilde{\mathbf{F}}_s = 0, \quad (20)$$

where \vec{F}_s is the heat flux in ice, written in the form

$$\vec{F}_s = \left(-k_s \frac{\partial \tilde{T}_s}{\partial \tilde{x}}, -k_s \frac{\partial \tilde{T}_s}{\partial \tilde{z}} \right) \quad (21)$$

with k_s and \tilde{T}_s denoting the heat conductivity of ice and the temperature in ice, respectively.

As described above, *Camporeale and Ridolfi* [2012] assumed that a constant heat flux penetrates the whole domain above the water-ice interface, because other choices do not make any significant difference in the instability characteristics. However, this assumption is not applicable to our analysis, in which the flow-ice interface is not in true equilibrium, as explained below. We assume that the heat flux from the flowing water to the water surface continuously matches that from the water surface to the ambient air. In order to make an accurate evaluation of the heat flux from the water surface to the surrounding air, the velocity and temperature distributions of air over the water surface must be obtained. We do not have such information, however, and therefore, we employ a simplification herein. The heat flux from the water surface to the ambient air is assumed to be expressed as $-\tilde{h}_t (\tilde{T}_a - \tilde{T}_f(\tilde{z} + \tilde{H}))$ with the use of a bulk heat transfer coefficient \tilde{h}_t . Therefore, the boundary condition for heat transfer at the water surface ($\tilde{z} = \tilde{z} + \tilde{H}$) is

$$\vec{F}_f \cdot \vec{e}_{ns} = -\tilde{h}_t (\tilde{T}_a - \tilde{T}_f) \quad \text{at} \quad \tilde{z} = \tilde{z} + \tilde{H}. \quad (22)$$

The estimation of the bulk heat transfer coefficient is discussed below. Meanwhile, the temperature at the bottom of the ice ($\tilde{z} = -\tilde{B}$) takes a constant value \tilde{T}_b , such that

$$\tilde{T}_s = \tilde{T}_b \quad \text{at} \quad \tilde{z} = -\tilde{B}, \quad (23)$$

where \tilde{B} is the ice thickness. At the interface between water and ice ($\tilde{z} = \tilde{z}$) where solidification and melting are taking place, the temperature at the interface is kept to the melting point \tilde{T}_m , such that

$$\tilde{T}_s = \tilde{T}_f = \tilde{T}_m \quad \text{at} \quad \tilde{z} = \tilde{z}. \quad (24)$$

We assume that the interface between water and ice is cooled from beneath and warmed from above, so that water at the interface is solidified and ice is melted at the same time. That is, the assumed conditions are

$$\tilde{T}_a > \tilde{T}_m > \tilde{T}_b. \quad (25)$$

The heat flux perpendicular to the water-ice interface is a scalar product of the heat flux vector and the unit vector normal to the water-ice interface $\vec{F}_s|_{\tilde{z}=\tilde{z}} \cdot \vec{e}_{nb}$. In a similar manner, the heat flux perpendicular to the interface is $\vec{F}_f|_{\tilde{z}=\tilde{z}} \cdot \vec{e}_{nb}$. The difference between the heat flux coming into the interface from ice below and the heat flux going out from the interface to the water above causes melting or solidification of water at the interface. This process is described by the relation

$$-\rho_s h_s \frac{\partial \tilde{z}}{\partial \tilde{t}} = \vec{F}_s|_{\tilde{z}=\tilde{z}} \cdot \vec{e}_{nb} - \vec{F}_f|_{\tilde{z}=\tilde{z}} \cdot \vec{e}_{nb}, \quad (26)$$

where h_s is the heat of melting and ρ_s is the density of ice [*Solari and Parker, 2013*].

3.4. Base State Normal Flow Solution

The base state for linear stability analysis is a flat bed and the normal flow condition, for which $\partial/\partial \tilde{x} = 0$ and $\tilde{w} = 0$. When the heat flux from ice to the water-ice interface is perfectly balanced with that from the interface to the flowing water above, neither solidification nor melting takes place, resulting in equilibrium. We should take this equilibrium state as a base state for a formal linear stability analysis. In order to apply the analysis to the experimental results, however, we relax this restriction and assume a more general case herein. The heat flux from the ice below is not necessarily balanced with that to water above, and the entire ice surface is moving upward or downward such that $\tilde{z} = \tilde{z}_0(t)$. At the same time, the water surface is moving with the ice surface such that $\tilde{z} = \tilde{H}_0 + \tilde{z}_0(t)$. With the use of a coordinate moving with the ice surface $\tilde{z}' = \tilde{z} - \tilde{z}_0(t)$, the locations of the ice and water surfaces are rewritten, respectively, in the forms

$$\tilde{z}' = 0, \quad (27)$$

$$\tilde{z}' = \tilde{H}_0. \quad (28)$$

The location of ice bottom is then expressed as

$$\tilde{z}' = -\tilde{B} - \tilde{Z}_0(t). \quad (29)$$

The implication is that while the locations of the ice and water surfaces do not change in the moving coordinate \tilde{z}' , the location of the ice bottom itself changes with time. Because the heat flux from ice to the water-ice interface changes depending on the location of the ice bottom, no steady state exists. We introduce the assumption $\tilde{B} > |\tilde{Z}_0(t)|$ so that the \tilde{z}' coordinate of the ice bottom location (thickness of ice) is approximated to be $-\tilde{B}$ (\tilde{B}). This is often referred to as the “frozen-time approximation” in linear stability analysis [Vesipa *et al.*, 2015; Camporeale, 2015].

With the use of \tilde{z}' (4) reduces, in the base state normal flow condition, to the following two equations:

$$g \sin \theta + \frac{d^2 \tilde{u}}{d\tilde{z}'^2} = 0 \quad (30)$$

$$-\frac{d\tilde{p}}{d\tilde{z}'} - g \cos \theta = 0. \quad (31)$$

The boundary conditions (8) and (15) reduce respectively to

$$\left. \begin{array}{l} \rho v \frac{d\tilde{u}}{d\tilde{z}'} = 0 \\ \tilde{p} = 0 \end{array} \right\} \text{ at } \tilde{z}' = \tilde{H}_0 \quad (32)$$

$$\tilde{u} = 0 \text{ at } \tilde{z}' = 0. \quad (33)$$

Solving (30) and (31) under the boundary conditions (32) and (33), we obtain the parabolic velocity distribution of laminar flow and the hydrostatic pressure distribution, such that

$$\tilde{u} = \frac{g \sin \theta}{\nu} \left(\tilde{H}_0 \tilde{z}' - \frac{1}{2} \tilde{z}'^2 \right) \quad (34)$$

$$\tilde{p} = g \cos \theta (\tilde{H}_0 - \tilde{z}'). \quad (35)$$

The heat transfer equations of water and ice are, respectively,

$$\frac{d^2 \tilde{T}_f}{d\tilde{z}'^2} = 0 \quad (36)$$

$$\frac{d^2 \tilde{T}_s}{d\tilde{z}'^2} = 0. \quad (37)$$

The boundary conditions for heat transfer are

$$-k_f \frac{d\tilde{T}_f}{d\tilde{z}'} = -\tilde{h}_t (T_a - T_f) \text{ at } \tilde{z}' = \tilde{H}_0 \quad (38)$$

$$\tilde{T}_f = \tilde{T}_m \text{ at } \tilde{z}' = 0 \quad (39)$$

$$\tilde{T}_s = \tilde{T}_m \text{ at } \tilde{z}' = 0 \quad (40)$$

$$\tilde{T}_s = \tilde{T}_b \text{ at } \tilde{z}' \approx -\tilde{B}. \quad (41)$$

Then, (36) and (37) have the solutions

$$\tilde{T}_f = \frac{\tilde{T}_a - \tilde{T}_m}{\tilde{H}_0 + k_f/\tilde{h}} \tilde{z}' + \tilde{T}_m \quad (42)$$

$$\tilde{T}_s \approx \frac{\tilde{T}_m - \tilde{T}_b}{\tilde{B}} z' + \tilde{T}_m. \quad (43)$$

Substituting the above equations into (26), we obtain the following relation:

$$\tilde{c} \approx \frac{1}{\rho_s h_s} \left(k_s \frac{\tilde{T}_m - \tilde{T}_b}{\tilde{B}} - k_f \frac{\tilde{T}_a - \tilde{T}_m}{\tilde{H}_0 + k_f/\tilde{h}} \right). \quad (44)$$

In the above equation, \tilde{c} is the aggradation/degradation speed of the ice surface defined by $\partial\tilde{Z}_0/\partial\tilde{t}$. In so far as the ice thickness \tilde{B} can be taken to be much larger than the increase in the thickness $\tilde{c}\tilde{t}$ ($\tilde{B} \gg \tilde{c}\tilde{t}$), the base state normal flow condition can be described by (34), (35), (42), and (43) with the velocity \tilde{c} satisfying (44).

3.5. Normalization

The dimensional variables with tildes are now made dimensionless by the use of the following transformations:

$$(\tilde{u}, \tilde{v}) = \tilde{U}_a (u, v), \quad (45)$$

$$(\tilde{x}, \tilde{z}') = \tilde{H}_0 (x, z), \quad (46)$$

$$\tilde{p} = \rho \tilde{U}_a^2 p, \quad (47)$$

$$\tilde{T}_f - \tilde{T}_m = (\tilde{T}_a - \tilde{T}_m) T_f, \quad (48)$$

$$\tilde{T}_s - \tilde{T}_m = (\tilde{T}_a - \tilde{T}_m) T_s, \quad (49)$$

$$\tilde{t} = \frac{\rho_s h_s \tilde{H}_0^2}{k_f (\tilde{T}_a - \tilde{T}_m)} t, \quad (50)$$

where the variables without tildes are the dimensionless versions of the corresponding variables. In the case of laminar flow, the following analytical relation holds

$$\tilde{U}_a = \frac{g \tilde{H}_0^2 \sin \theta}{3\nu}. \quad (51)$$

With the use of (45) to (51), (4) and (5) reduce to

$$(\mathbf{u} \cdot \nabla) \mathbf{u} = -\nabla p + \frac{1}{Re} (\mathbf{g} + \nabla^2 \mathbf{u}) \quad (52)$$

$$\nabla \cdot \mathbf{u} = 0, \quad (53)$$

where Re is the Reynolds number and \mathbf{g} is the normalized gravity vector, written, respectively, in the forms

$$Re = \frac{\tilde{U}_a \tilde{H}_0}{\nu}, \quad (54)$$

$$\mathbf{g} = \left(3, -\frac{3}{\tan \theta} \right). \quad (55)$$

We introduce the stream function ψ defined by

$$(u, w) = \left(\frac{\partial \psi}{\partial z}, -\frac{\partial \psi}{\partial x} \right). \quad (56)$$

Then, the x and z components of (52) are rewritten, respectively, in the forms

$$\frac{\partial \psi}{\partial z} \frac{\partial^2 \psi}{\partial x \partial z} - \frac{\partial \psi}{\partial x} \frac{\partial^2 \psi}{\partial z^2} = -\frac{\partial p}{\partial x} + \frac{1}{Re} \left(3 + \frac{\partial^3 \psi}{\partial x^2 \partial z} + \frac{\partial^3 \psi}{\partial z^3} \right) \quad (57)$$

$$-\frac{\partial \psi}{\partial z} \frac{\partial^2 \psi}{\partial x^2} + \frac{\partial \psi}{\partial x} \frac{\partial^2 \psi}{\partial x \partial z} = -\frac{\partial p}{\partial z} - \frac{1}{Re} \left(\frac{3}{\tan \theta} + \frac{\partial^3 \psi}{\partial x^3} + \frac{\partial^3 \psi}{\partial x \partial z^2} \right). \quad (58)$$

Eliminating p in the above equations, we obtain

$$\frac{\partial \psi}{\partial z} \frac{\partial \nabla^2 \psi}{\partial x} - \frac{\partial \psi}{\partial x} \frac{\partial \nabla^2 \psi}{\partial z} - \frac{1}{Re} \nabla^2 \nabla^2 \psi = 0 \quad (59)$$

The boundary conditions for the flow (8) and (15) are normalized to the forms

$$\left. \begin{aligned} \mathbf{u} \cdot \mathbf{e}_{ns} &= 0 \\ \mathbf{e}_{ts} \cdot \mathbf{T} \cdot \mathbf{e}_{ns} &= 0 \\ \mathbf{e}_{ns} \cdot \mathbf{T} \cdot \mathbf{e}_{ns} &= 0 \end{aligned} \right\} \text{ at } z = Z + H \quad (60)$$

$$\left. \begin{aligned} \mathbf{u} \cdot \mathbf{e}_{tb} &= 0 \\ \mathbf{u} \cdot \mathbf{e}_{nb} &= 0 \end{aligned} \right\} \text{ at } z = Z. \quad (61)$$

Equations (18) and (20) are normalized, respectively, to the forms

$$\frac{\partial \psi}{\partial z} \frac{\partial T_f}{\partial x} - \frac{\partial \psi}{\partial x} \frac{\partial T_f}{\partial z} = \frac{1}{Re Pr} \left(\frac{\partial^2 T_f}{\partial x^2} + \frac{\partial^2 T_f}{\partial z^2} \right) \quad (62)$$

$$\frac{\partial^2 T_f}{\partial x^2} + \frac{\partial^2 T_f}{\partial z^2} = 0, \quad (63)$$

where Pr is the Prandtl number, defined as

$$Pr = \frac{\nu}{k_f / \rho c_v}. \quad (64)$$

While in general the Prandtl number is a variable, here we have set it equal to the value 13.52 corresponding to water flow on ice.

The boundary conditions for temperature (22) to (24) reduce to

$$\mathbf{F}_f \cdot \mathbf{e}_{ns} = -h_t (1 - T_f) \quad \text{at } z = H \quad (65)$$

$$T_f = 0 \quad \text{at } z = Z \quad (66)$$

$$T_s = 0 \quad \text{at } z = Z \quad (67)$$

$$T_s = T_b \quad \text{at } z = -B, \quad (68)$$

where $h_t = \tilde{h}_t \tilde{H}_0 / k_f$ and $T_b = (\tilde{T}_b - \tilde{T}_m) / (\tilde{T}_a - \tilde{T}_m)$.

The normalized form of the time variation of the ice surface elevation (26) is [Solari and Parker, 2013]

$$-\frac{\partial Z}{\partial t} = \lambda \mathbf{F}_s|_{z=Z} \cdot \mathbf{e}_{nb} - \mathbf{F}_f|_{z=Z} \cdot \mathbf{e}_{nb}, \quad (69)$$

where λ is the ratio of the heat conductivity of ice k_s to that of water k_f ($= k_s / k_f$), and the normalized heat flux in water \mathbf{F}_f and that in ice \mathbf{F}_s are respectively written in the forms

$$\mathbf{F}_f = \left(-\frac{\partial T_f}{\partial x}, -\frac{\partial T_f}{\partial z} \right) \quad (70)$$

$$\mathbf{F}_s = \left(-\frac{\partial T_s}{\partial x}, -\frac{\partial T_s}{\partial z} \right). \quad (71)$$

3.6. Linear Stability Analysis

A small perturbation is imposed on the base state normal flow condition. With the use of the amplitude A , wave number α , complex angular frequency ω of a perturbation, all the variables are expanded in the following forms:

$$\psi = \psi_0(z) + A\psi_1(z) e^{i(\alpha x - \omega t)}, \quad (72)$$

$$p = p_0(z) + Ap_1(z) e^{i(\alpha x - \omega t)}, \quad (73)$$

$$T_f = T_{f0}(z) + AT_{f1}(z) e^{i(\alpha x - \omega t)}, \quad (74)$$

$$T_s = T_{s0}(z) + AT_{s1}(z) e^{i(\alpha x - \omega t)}, \quad (75)$$

$$H = 1 + AH_1 e^{i(\alpha x - \omega t)}, \quad (76)$$

$$Z = AZ_1 e^{i(\alpha x - \omega t)}, \quad (77)$$

where the subscripts 0 and 1 indicate variables at $O(1)$ and $O(A)$, respectively. Substituting these expansions into (57), (58), (62), and (63), we obtain a series of equations at $O(1)$. We solve those equations to obtain the solutions at $O(1)$ under the boundary conditions specified above. The solutions are

$$\psi_0 = \frac{3}{2}z \left(z - \frac{1}{3}z^2 \right), \quad (78)$$

$$p_0 = \frac{3}{Re \tan \theta} (1 - z), \quad (79)$$

$$T_{f0} = \frac{h_t}{1 + h_t} z, \quad (80)$$

$$T_{s0} = -\frac{T_b}{B} z, \quad (81)$$

$$c = \lambda \left(-\frac{T_b}{B} - \frac{h_t}{1 + h_t} \right). \quad (82)$$

These solutions correspond to normalized versions of the base state normal flow solutions (34), (35), (42), and (43).

Substituting (72) to (77) into (59), and collecting terms at $O(A)$, we obtain

$$\psi_1^{iv} + (i\alpha Re u_0 - 2\alpha^2) \psi_1'' - [i\alpha Re(\alpha^2 u_0 + u_0'') + \alpha^4] \psi_1 = 0, \quad (83)$$

where \prime denotes $\partial/\partial z$, u_0 is the nondimensional streamwise velocity in the base state ($= \psi_0'$). At $O(A)$, the boundary conditions (60) and (61) reduce to

$$\psi_1(1) + u_0(1)H_1 = 0, \quad (84)$$

$$\alpha^2 \psi_1(1) + \psi_1''(1) + u_0''(1)H_1 = 0, \quad (85)$$

$$Re [p_1(1) + p_0'(1)H_1] + 2i\alpha [\psi_1'(1) + u_0'(1)H_1] = 0, \quad (86)$$

$$\psi_1'(0) + u_0'(0)Z_1 = 0, \quad (87)$$

$$\psi_1(0) + u_0(0)Z_1 = 0. \quad (88)$$

In the above equations, $p_1(1)$ can be obtained by an equation at $O(A)$ obtained from (57) evaluated when $z = 1$.

$$p_1(1) = u'_0(1)\psi_1 - \left[u_0(1) - \frac{\alpha}{Re} \right] \psi'_1(1) + \frac{\psi'''_1(1)}{Re}. \quad (89)$$

Equation (83) is a fourth-order differential equation in ψ_1 , and (84) to (88) include two additional unknown variables H_1 and Z_1 , while (84) to (89) provide five boundary conditions. Therefore, ψ_1 and H_1 can be expressed by the following forms:

$$\psi_1(z) = \hat{\psi}_1(z)Z_1, \quad (90)$$

$$H_1 = \hat{H}_1Z_1. \quad (91)$$

From (62) and (63), we obtain the following equations at $O(A)$, respectively:

$$\alpha (i Re Pr u_0 + \alpha) T_{f1} - i\alpha Re Pr T'_{f0} \psi_1 - T''_{f1} = 0, \quad (92)$$

$$-\alpha^2 T_{s1} + T''_{s1} = 0. \quad (93)$$

From the boundary conditions for heat transfer (65) to (68), we obtain the following equations at $O(A)$:

$$T'_{f1}(1) = h_t [T_{f1}(1) + T'_{f0}(1)H_1], \quad (94)$$

$$T_{f1}(0) + T'_{f0}(0)Z_1 = 0, \quad (95)$$

$$T_{s1}(0) + T'_{s0}(0)Z_1 = 0, \quad (96)$$

$$T_{s1}(-B) = 0. \quad (97)$$

Equations (92) and (93) are the governing second order differential equations for T_{f1} and T_{s1} , respectively, and can be solved under the boundary conditions (94) to (97). Because (94) to (96) include H_1 and Z_1 , T_{f1} and T_{s1} can be written in the following forms:

$$T_{f1}(z) = \hat{T}_{f1}(z)Z_1, \quad (98)$$

$$T_{s1}(z) = \hat{T}_{s1}(z)Z_1. \quad (99)$$

There is an analytical solution for $\hat{T}_{s1}(z)$, which takes the form

$$\hat{T}_{s1} = \alpha \frac{T_b}{B} \coth(\alpha B). \quad (100)$$

The time variation of the ice surface elevation (69) can be expanded in the form

$$i\omega Z_1 + \lambda T'_{s1}(0) - T'_{f1}(0) = 0. \quad (101)$$

Substituting (98) and (99) into the above equations, we obtain ω in the following form:

$$\omega = i (\lambda \hat{T}'_{s1}(0) - \hat{T}'_{f1}(0)). \quad (102)$$

Because the differential equations (83) and (92) are linear, but their coefficients are functions of z , they cannot be solved analytically. *Camporeale and Ridolfi* [2012] employed a semianalytical method with the use of a Frobenius expansion. We instead employ a spectral collocation method using Chebyshev polynomials herein.

3.7. Results of the Analysis: α -RePlane

The neutral stability curves ($\text{Im}[\omega] = 0$) in the α -Re plane obtained from the analysis are shown in Figure 11. In all cases, the region outside the zone bounded by the neutral curves corresponds to the region where

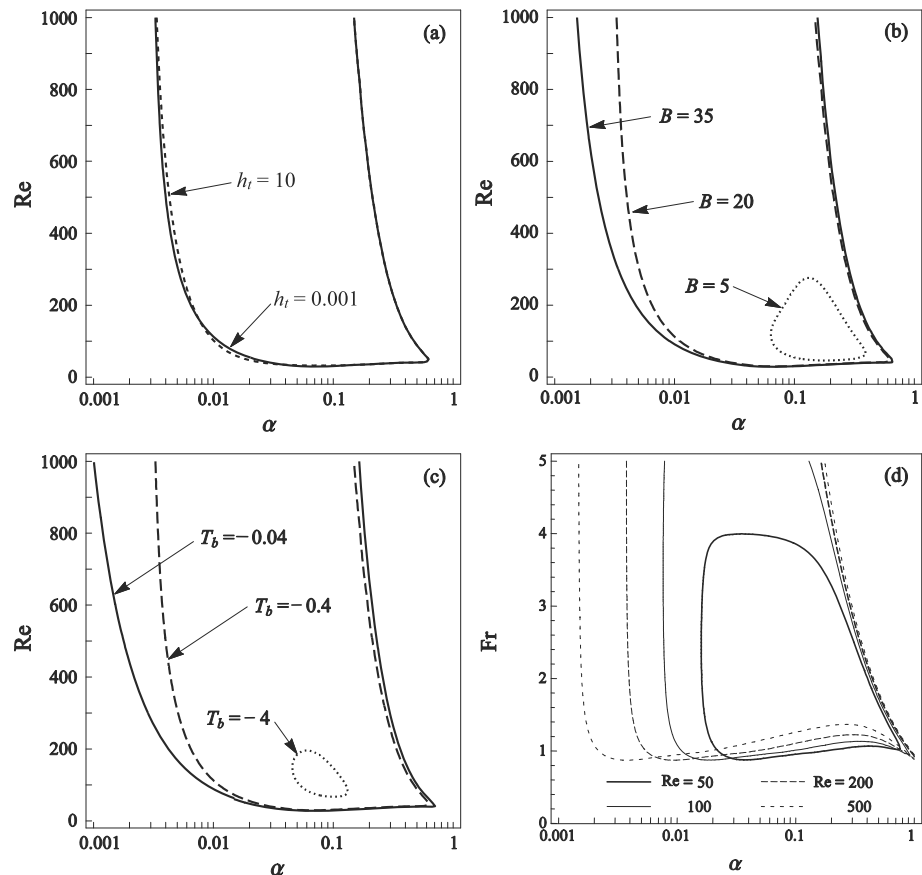


Figure 11. Instability diagrams for the cases (a) $T_b = -0.4$, $B = 20$, $\theta = 5^\circ$, (b) $h_t = 0.01$, $T_b = -0.4$, $\theta = 5^\circ$, (c) $h_t = 0.01$, $B = 20$, $T_b = -0.4$, and (d) $h_t = 0.01$, $B = 20$, $\theta = 5^\circ$. Numbers on contours are values of growth rate of perturbation. Figures 11a–11c show almost the same results as those obtained by *Camporeale and Ridolfi* [2012] except for the spike in the solid line in the range of small Re and large α . This may be due to the neglect of surface tension in this analysis. In the range of the data observed in the experiments, the effect of surface tension can be neglected in the analysis.

$\text{Im}[\omega] < 0$, so that the flat bed is stable, while the region inside the zone bounded by the curves for neutral stability correspond to the region where $\text{Im}[\omega] > 0$, so that the flat bed is unstable. In the analysis of *Camporeale and Ridolfi* [2012], who used the precise equilibrium base state and the assumption of constant heat flux, the Reynolds number Re , the slope angle θ , and the water surface temperature are important parameters that can be freely and independently changed. However, in our analysis with the use of the frozen-time approximation, as well as the thermal boundary condition at the water surface described by the bulk heat transfer coefficient, there are more free parameters. More specifically, Re , θ , h_t , B , and T_b are all free and independent parameters. In so far as the effect of the slope angle θ has been already discussed by *Camporeale and Ridolfi* [2012], we choose h_t , B , and T_b to study the effects of variation of these parameters, as outlined subsequently.

In Figure 11a, we study the effect of heat transfer from the water surface to the ambient air on the instability of the water-ice interface. There have been many studies on the heat transfer coefficient \tilde{h}_t in mechanical engineering, but most of them focus on the heat transfer from a solid surface to a fluid. In oceanography or geophysics, the bulk heat transfer coefficient of air above the sea surface is commonly expressed as

$$\tilde{h}_t = \rho_a C_{pa} C_H U_{10}, \tag{103}$$

where ρ_a is the air density, which is 1.293 kg/m^3 at 0°C and 1 atm, C_{pa} is the specific heat of air, which is 1.005 J/kgK , C_H is a nondimensional heat transfer coefficient, and U_{10} is the wind velocity at the height of 10 m above the sea surface. According to a number of field observations, the nondimensional heat transfer coefficient is found to range from 0.6×10^{-3} to 1.4×10^{-3} when U_{10} is smaller than 10 m/s [*Kondo*, 1975; *Garratt and Hyson*, 1975; *Friehe and Schmitt*, 1976; *Smith*, 1980; *Large and Pond*, 1982]. *Komori et al.* [2011] have performed experiments using a wind-wave tank and found that C_H is slightly smaller than that in the field

but still in the range of the observed field data. In our experiments, which were conducted in a small cold chamber, it is rather difficult to determine U_{10} . As explained previously, the temperature of the cold chamber is controlled by an air conditioner, so that the room air is forced to flow at a relatively high speed. We assume that the smallest and largest possible wind speeds equivalent to U_{10} are 1 m/s and 10 m/s, respectively. The thermal conductivity of water k_f is 0.6 W/mK. If we estimate the flow depth to be 0.001 to 1 m considering the range applicable to the experiments and the field, the normalized bulk heat transfer coefficient h_t is found to range from 0.0012 to 29. The neutral curves corresponding to the cases $h_t = 0.001$ and 10 are shown by the solid and dashed lines in Figure 11a, in which $\theta=5^\circ$, $T_b = -0.4$, and $B = 20$. It is notable that the large difference in h_t results only in a slight difference between the neutral curves. This is probably because of the linearity of the thermal boundary condition at the water surface, as noted by *Camporeale and Ridolfi* [2012]. We employ the value of 1 as the normalized heat transfer coefficient h_t for the analysis below.

Figure 11b shows the neutral curves when $h_t = 1$, $\theta=5^\circ$, and $T_b = -0.4$. The dotted, dashed, and solid lines in the figure correspond to the cases for which $B = 5, 20$, and 35 , respectively. Figure 11c shows the neutral curves when $h_t = 1$, $\theta=5^\circ$, and $B = 20$. The solid, dashed, and dotted lines are the neutral curves for the cases for which $T_b = -0.04, -0.4$, and -4 , respectively. According to the figures, the unstable region expands with increasing nondimensional ice thickness B and ice bottom temperature T_b but does not show significant changes when B is larger than 20 or T_b is larger than -0.4 . This is because the heat flux from the ice stabilizes the flow-ice interface. As seen in (100), the magnitude of heat flux from the ice declines with increasing B and T_b .

3.8. Results of the Analysis: α -FrPlane

Figures 11a and 11b obscure an important aspect of the stability analysis. In the case of laminar open channel flow, the Reynolds number Re and the Froude number Fr are related in a very specific way:

$$Fr = \sqrt{\frac{Re \sin \theta}{3}}. \quad (104)$$

It is thus possible to replot the stability diagrams of Figures 11a and 11b on the α -Fr plane. As shown in Figures 11d, the instability studied here appears only within the range of Froude-supercritical flows, i.e., within the range $Fr > 1$. This is the basis for our identification of this instability as the open channel water-ice equivalent of the antidune instability of open channel flow over sand.

4. Discussion

4.1. Comparison Between Experiments and Theory

Let us investigate whether or not the cyclic steps reproduced in the experiments can be explained at least in part by the above linear stability analysis of a water-ice interface below a free water surface. Figure 12a is a diagram in which the contours of the growth rate of the perturbation $\text{Im}[\omega]$ obtained in the linear stability analysis and the experimental data are both plotted on the α - Re plane. The figure pertains to the case for which the slope angle θ is 5° . Among the experimental cases, B and T_b are all different, and therefore, each experimental data point corresponds to a different group of contours. In the figure, the contours of the most stable case of the four experimental cases, in which $T_b = -0.54$ and $B = 26$, are plotted with solid lines, and the contours of the most unstable case, in which $T_b = -0.18$ and $B = 41$, are plotted with dashed lines. Open circles show the experimental data for which cyclic steps formed, and which also had a Reynolds number smaller than 750, here taken to be the critical value for the laminar-turbulent transition [*Lajeunesse et al.*, 2010]. It is found that the dominant wave number associated with the maximum growth rate is approximately 0.3 when the Reynolds number is around 100: this growth rate decreases down to 0.08 with increasing Reynolds number.

The wave numbers observed in the experiments take rather small values, i.e., from 0.01 to 0.03. This is not surprising. As described above, the linear analysis presented here can only capture the initial instability leading to the water-ice analog of antidunes; cyclic steps themselves cannot be described in terms of a linear stability analysis. In so far as cyclic steps are long-wave relatives of antidunes, however, it is of value to know that the experimental flow conditions do indeed fall within the range of the antidune instability. In addition, it can be seen from Figures 12 and 13 that all the experimental data in which cyclic steps formed appear in the range for which the flat ice surface is subject to the ice analog of antidune instability presented here.

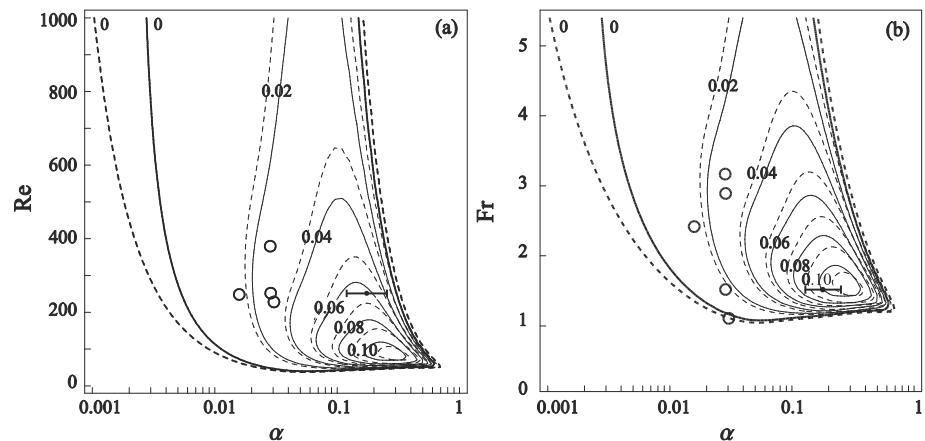


Figure 12. Comparison between the experimental results and the analytical results for the case $\theta=5^\circ$ in (a) the α - Re plane and (b) the α - Fr plane. The numbers on the contours are values of perturbation growth rate. The wavenumbers determined from the wavelengths of small undulations on the water surface, which are considered to be “in-phase” waves of harbinger antidune-like bedforms, are plotted as error bars (see 4.1 for an explanation).

Figure 12b is a diagram in which the contours of the growth rate $\text{Im}[\omega]$ in Figure 12a are replotted in the α - Fr plane with the use of (104), and the experimental data are replotted by the open circles. Note that the Reynolds number calculated by the measured discharge, and the Froude number calculated by the measured discharge and flow depth pertaining to each experimental datum does not necessarily satisfy the relation (104). This is because the measured flow depth does not necessarily equal the predicted flow depth. In the derivation of (104), the channel is assumed to be infinitely wide, and the velocity distribution is assumed to be described by (34). In the experiments, however, the channel is sufficiently narrow to feel the effect of side walls, and slight roll waves take place on the water surface, as described previously. These factors could cause the Reynolds and Froude numbers to fail to satisfy the relation (104). As shown in Figure 12b, all the experimental data points are located in the range of instability, except for one data point on the neutral curve.

Figure 13a is a diagram for the case for which $\theta = 20^\circ$. In that figure the contours of the growth rate $\text{Im}[\omega]$ obtained from the analysis and the experimental data are plotted in the α - Re plane. In this figure as well, the contours of the growth rate in the most stable case are shown by the solid lines, those in the most unstable case are shown by the dashed lines, and the experimental data with cyclic steps formed are shown by the open circles. Figure 13b shows the contours of the growth rate and the experimental data replotted in the α - Fr plane. It is found that the wave numbers observed in the experiments are smaller than the dominant wave numbers obtained from the stability analysis, though all the experimental data for the cyclic steps are located in the range of instability.

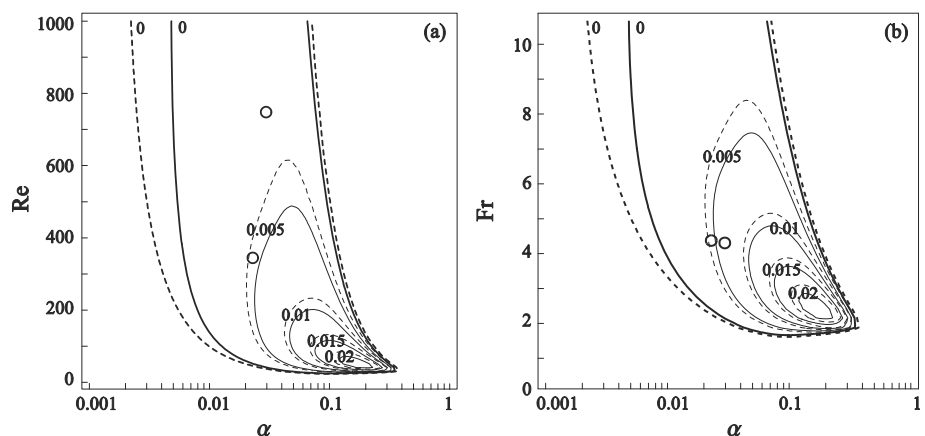


Figure 13. Comparison between experimental results and analytical results for the case $\theta=20^\circ$ in (a) the α - Re plane and (b) the α - Fr plane.

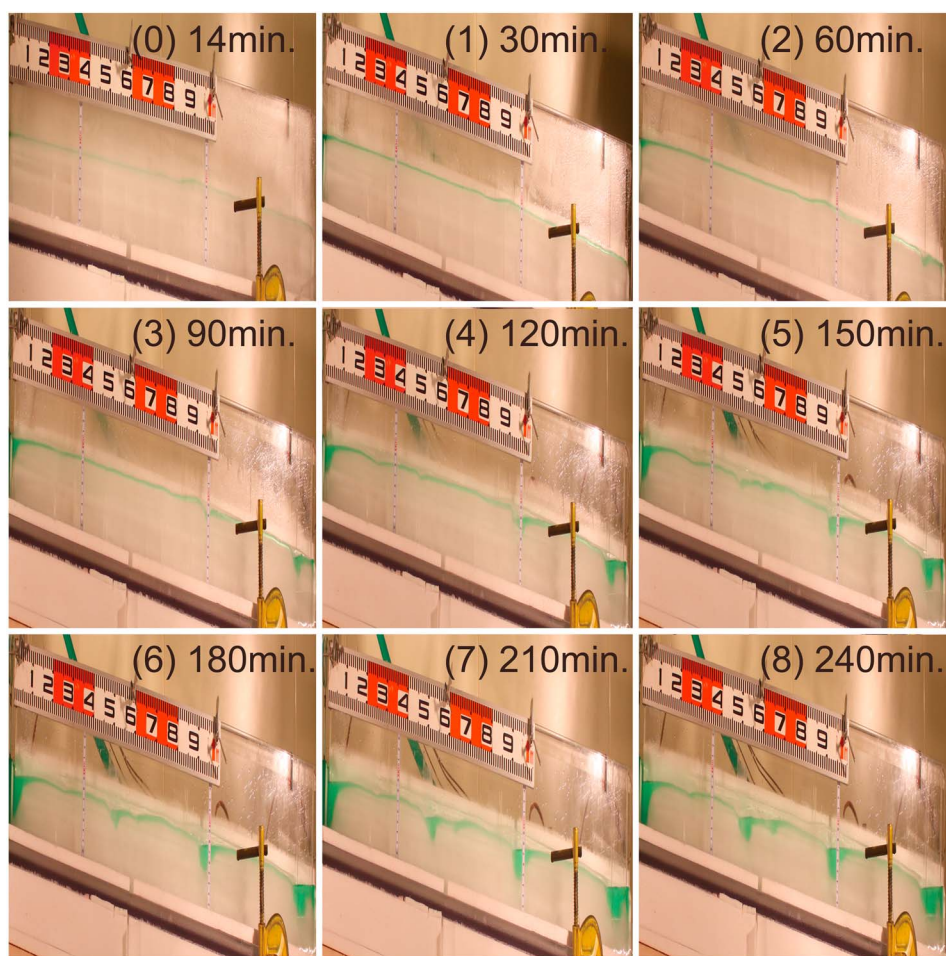


Figure 14. Sequential images of CSIM120908A $\times 5$ in the vertical direction. Numbers in parentheses correspond to those of Figure 8. Small “in-phase” wave-like undulations can be seen when the ice surface starts melting approximately 1 h after the beginning of the run ((2) and (3)). Water surface waves with wavelengths of approximately 5 to 10 cm are observed around 90 min after the beginning of the run (3). From 120 min subsequent to the beginning of the run, these undulations become rather ill-defined, and deeper, longer-spaced depressions appear (4). These depressions appear to evolve into steps after 150 min (5). They become fully developed steps after 180 to 240 min ((6)–(8)).

The question arises as to whether or not precursor antidunes with shorter wavelengths can be observed before the development of steps. The preceding “bedforms” on ice cannot be clearly be recognized in the photographs taken through the sidewalls of Plexiglas. One reason for this is probably because the amplitude of these harbinger bedforms may be too small to be observed. Another reason may be that the ice tended to start melting in a zone that was narrower than the full flume width. Because of this, sometimes the shape of the initially formed perturbation on ice may not be expressed along the sidewalls, so that small-amplitude waves cannot be resolved visually. If the harbinger bedforms are antidunes, however, the amplitude of the water surface waves should be in most cases significantly larger than that of the bed waves. We, therefore, focus on the displacement of the water surface instead of the ice surface.

The sequential images of CSIM120908A $\times 5$ in the vertical direction are shown in Figure 14. Small “in-phase” wave-like undulations can be seen when the ice surface starts melting approximately 1 h after the beginning of the run (Figure 14, (2) and (3)). In the case of Figure 14, water surface waves with wavelengths of approximately 5 to 10 cm are predominantly observed around 90 min after the beginning of the run (Figure 14, (3)). Then, after 120 min from the beginning, these undulations become rather unclear, and deeper, longer-spaced depressions appear (Figure 14, (4)). These depressions appear to evolve into steps after 150 min (Figure 14, (5)). They become fully developed steps after 180 to 240 min (Figure 14, (6)–(8)). This example is a rather rare experimental case for which slight undulations can be recognized both on the water and ice surfaces. Though

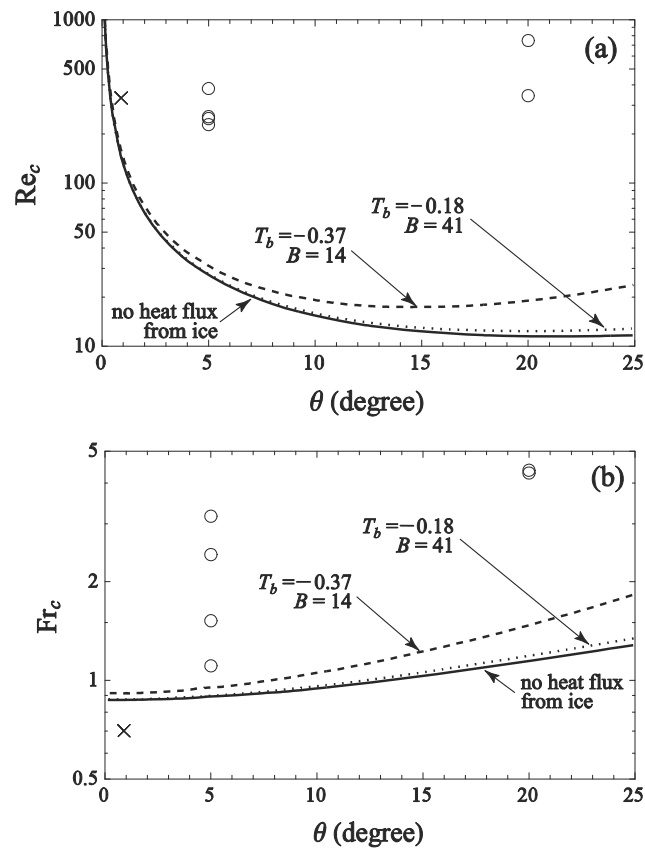


Figure 15. Unstable and stable regions and experimental data in (a) the slope angle-Reynolds number domain and (b) the slope angle-Froude number domain. The solid, dashed, and dotted lines correspond to the boundaries between unstable and stable regions in the case with no heat flux from ice, and the cases $(T_b, B) = (-0.18, 41)$ and $(-0.37, 14)$, respectively. The circles and crosses correspond to the experimental data with and without the formation of cyclic steps, respectively.

clear antidune-like undulations cannot be recognized on the ice surface in the other experimental cases, small undulations of the water surface can nevertheless be observed in some of these cases.

The wave numbers determined from the wavelengths of small undulations on the water surface are plotted in Figure 12. The wavelengths cannot be precisely determined so the data are plotted as error bars. It is seen that from the figures that data cover the range close to the dominant wave numbers associated with maximum growth rates. This suggests that the small antidune-like undulations observed before steps are formed are likely precursors of ice steps.

4.2. The Critical Reynolds and Froude Numbers

Figures 15a and 15b show the critical Reynolds number and the critical Froude number as functions of slope angle θ . The solid lines correspond to the case for which there is no heat flux from ice, the dotted lines to the most unstable case, for which $T_b = -0.37$ and $B = 14$ in all the experimental cases, and the dashed lines to the most stable case, for which $T_b = -0.18$ and $B = 41$. In the figure, the open circles indicate the experimental data for which cyclic steps formed, while the single cross indicates the experiment for which steps did not form. In the upper regions within the solid, dotted, or dashed lines, the flat ice surface becomes unstable, and in the lower region outside these lines, the flat surface remains stable. In Figure 15a, where the stability curves are expressed in terms of the Reynolds number, all the experimental data are found to plot in the unstable region. This notwithstanding the data for which steps did not form is located close to the boundary between the stable and unstable regions. Meanwhile, in Figure 15b, where the curves are expressed in terms of the Froude number, all the experimental data for which steps formed plot in the upper unstable region, and the one data point corresponding to the absence of step formation plots in the lower stable region. It is found that the experimental results are thus well explained in terms of the critical Froude number.

Note that because the Reynolds and Froude numbers of the data in Figures 15a and 15b respectively do not necessarily satisfy the relation (104), as already explained, there is a datum which falls on the unstable region in the θ - Fr plane but falls on the stable region in the θ - Re plane.

4.3. Propagation and Expansion of Steps

In most cases of our experiments, when the ice surface does not have significant irregularities or defects and is almost perfectly flat at the beginning of the experiment, a step formed just upstream of the downstream weir, and another step formed some distance upstream, so that the disturbance due to the effect of the downstream step propagated in the upstream direction (see 2.2.3, Figure 8). This process was repeated until the whole ice surface was covered with steps. As described in 2.2.2, in most cases, the depressions themselves expand in the upstream direction. This can be explained as follows. Water flows down the upstream shallow part of the depression as a supercritical flow in the Froude sense and flows down the downstream deeper part as a subcritical flow (Figure 7). A hydraulic jump takes place between the upstream shallow part and the downstream deeper part. Therefore, the ice bed in the shallower supercritical slope reach is more affected by high atmospheric temperature than that in the deeper subcritical slope reach. This might explain the upstream expansion of the depression.

According to the theoretical analysis of *Camporeale and Ridolfi* [2012], an unstable flat interface evolves into a train of waves migrating in the upstream direction if the water temperature is higher than the ice and lower than the ambient air. Our analysis is in agreement with this result, although we do not explicitly illustrate this herein. The experimental results are thus consistent with the analytical results. Our treatment cannot be immediately applied to the spiral troughs of Mars formed by a katabatic wind including a small amount of water vapor. However, we can say that the observations of the experiments and the result of the analysis are consistent with the growth process of the spiral troughs on Mars proposed by *Smith et al.* [2013] on the basis of the depositional structure under the ice surface (see their Figure 2).

Some depressions are nevertheless observed to expand toward the downstream direction in these experiments. This might be an effect of turbulent mixing which is not considered in the theory described above. Turbulent mixing is activated in deep depressions by hydraulic jumps. It may be the case that the relatively high temperature of the ambient air is efficiently transported to the deep, downstream part of the depressions, so as amplify the melting rate there.

The present study shows that a series of steps can form on the interface between ice and fluid flowing adjacent it due to thermal as well as mechanical processes. This provides strong support for the interpretation of *Smith et al.* [2013] that the spiral troughs on Mars are indeed cyclic steps. The experimental conditions of this study are dominated by differential melting rather than differential freezing or spatially alternating melting and freezing. In this sense, they may be close to the conditions of the South Polar Ice Cap of Mars, where erosional-dominated cyclic steps thought to be created by katabatic winds are observed [*Smith et al.*, 2014]. The results of this study also provide a physical explanation for the formation of ice steps on a relatively steep bed surface of a supraglacial meltwater stream, as shown in Figure 1b.

5. Conclusions

In this study, we performed flume experiments to reproduce cyclic steps formed on ice due to the spatial nonuniformity of melting and solidification caused by flowing water. Our experiments were conducted under the condition that temperature increases in the following order: ice < flowing water < surrounding air. As a result, we found that trains of steps are formed in ice when the Froude number is larger than a value around unity. In the developed state, these steps were found to correspond to long waves, in the sense that the dimensionless wave numbers based on flow depth were observed to be small. In addition, the steps were delineated by hydraulic jumps. Finally, most steps in ice expanded in the upstream direction, although some steps were observed to expand downstream. The three characteristics of (a) long wavelength relative to depth, (b) upstream migration, and (c) the presence of trains of hydraulic jumps are diagnostic of cyclic steps in sand. With this in mind, the upstream-expanding steps that we observed can be identified as cyclic steps formed on an ice bed.

We performed a linear stability analysis to investigate the instability of the interface between flowing water and ice and obtained a partial physical explanation of the formation of cyclic steps. More specifically, we verified the existence of a Froude-supercritical instability mechanism for open channel water-ice interfaces that

is analogous to the antidune instability over a sand bed. Cyclic steps are not directly amenable to linear stability analysis, but the base flow for cyclic steps is known to also satisfy the antidune instability [e.g., *Parker and Izumi, 2000*]. Our analysis is essentially similar to *Camporeale and Ridolfi's [2012]*, but some modification is made in the thermodynamic boundary condition at the water surface in order to apply the analysis to the experiments. According to the results of the analysis, the interface becomes unstable when the Reynolds number is relatively large, under the conditions that the heat flux from ice is sufficiently weak, i.e., when the temperature at the ice bottom is not too low compared to freezing, and that the ice thickness is sufficiently large. In addition, the unstable region in the wave number- Reynolds number plane only weakly depends on (a) the heat transfer coefficient of air normalized by the heat diffusivity of water and (b) the flow depth.

We compared the results of experiments and the analysis and found that the experimental data fall in the unstable region both in the wave number-Reynolds number plane and the wave number-Froude number plane, i.e., where the analysis predicts interfacial instability. The wave numbers observed in the experiments are, however, one order smaller than the dominant wave numbers predicted by the analysis. We found that small harbinger antidune-like bedforms appear before well-defined steps are formed. The wave numbers of these precursor bedforms are comparable with the dominant wave number predicted by the analysis. This indicates that at least the experimental results are consistent with the analytical results. In addition, we plotted the experimental data on the predicted diagrams of the critical Reynolds number and the critical Froude number, both as functions of slope angle. We found that when plotted on the theoretical diagram describing the critical Reynolds number, all the data for which steps formed fall in the unstable region of Reynolds number, i.e., above the critical Reynolds number. Though the data for which steps do not form fall in the unstable region as well, they are located close to the border between stable and unstable regions. This discrepancy may be due in part to the fact that the experimental data pertain to a high-amplitude phenomenon, whereas the analysis pertains to infinitesimal bed perturbations. This discrepancy might be overcome by means of a weakly nonlinear stability analysis or full nonlinear analysis [*Parker and Izumi, 2000; Colombini and Stochino, 2008*]. The critical Froude number derived from the analysis is approximately unity in the range of small slope angles and increases slightly with slope angle. In the experiments, cyclic steps did not form in the case of a Froude number smaller than unity, whereas cyclic steps formed in all cases for which the Froude number was larger than unity. In terms of the critical Froude number, then, the experimental results are well explained by the analysis.

Notation

A	amplitude of perturbation;
\tilde{B}, B	dimensional and nondimensional ice thicknesses, respectively;
\tilde{c}, c	dimensional and nondimensional moving speeds of the ice surface, respectively;
C_{pa}	specific heat of air;
C_H	nondimensional heat transfer coefficient;
C_v	specific heat of water;
$\tilde{\mathbf{e}}_{ts}, \mathbf{e}_{ts}$	dimensional and nondimensional unit vectors tangential to the water surface, respectively;
$\tilde{\mathbf{e}}_{ns}, \mathbf{e}_{ns}$	dimensional and nondimensional unit vectors normal to the water surface, respectively;
$\tilde{\mathbf{e}}_{tb}, \mathbf{e}_{tb}$	dimensional and nondimensional unit vectors tangential to the ice surface, respectively;
$\tilde{\mathbf{e}}_{nb}, \mathbf{e}_{nb}$	dimensional and nondimensional unit vectors normal to the ice surface, respectively;
Fr	Froude number;
$\tilde{\mathbf{F}}_f, \mathbf{F}_f$	dimensional and nondimensional heat fluxes in water, respectively;
$\tilde{\mathbf{F}}_s, \mathbf{F}_s$	dimensional and nondimensional heat fluxes in ice, respectively;
$\tilde{\mathbf{g}}, \mathbf{g}$	dimensional and nondimensional gravitational acceleration vectors, respectively;
g	gravitational acceleration ($= 9.8 \text{ m/s}^2$);
\tilde{H}, H	dimensional and nondimensional flow depths, respectively;
\tilde{H}_0	flow depth in the initial flat bed normal flow condition;
\tilde{h}_t, h_t	dimensional and nondimensional bulk heat transfer coefficients, respectively;
h_s	heat of melting;
k_f	heat conductivity of water;
k_s	heat conductivity of ice;
\tilde{L}, L	dimensional and nondimensional wavelengths of boundary waves, respectively;
\tilde{p}, p	dimensional and nondimensional pressures, respectively;

Pr	Prandtl number;
Re	Reynolds Number;
$\tilde{\mathbf{T}}, \mathbf{T}$	dimensional and nondimensional stress tensors, respectively;
\tilde{T}_a	room temperature;
\tilde{T}_b, T_b	dimensional and nondimensional ice bottom temperatures, respectively;
\tilde{T}_f, T_f	dimensional and nondimensional water temperatures, respectively;
\tilde{T}_m	melting temperature;
\tilde{T}_s, T_s	dimensional and nondimensional ice temperatures, respectively;
\tilde{U}_a	depth-averaged velocity in the base state normal flow condition;
U_{10}	wind velocity at the height of 10 m above the sea surface;
$\tilde{\mathbf{u}}, \mathbf{u}$	dimensional and nondimensional velocity vectors, respectively;
\tilde{u}, u	dimensional and nondimensional velocity components in the streamwise direction, respectively;
\tilde{w}, w	dimensional and nondimensional velocity components in the upward normal direction, respectively;
\tilde{x}, x	dimensional and nondimensional coordinates in the streamwise direction, respectively;
\tilde{z}, z	dimensional and nondimensional coordinates in the upward normal direction, respectively;
\tilde{Z}, Z	dimensional and nondimensional ice surface elevations, respectively;
\tilde{Z}_0	ice surface elevation in the initial flat bed normal flow condition;
\tilde{z}', z'	dimensional and nondimensional coordinates in the upward normal direction moving with the ice surface, respectively;
α	wave number of perturbation;
$\tilde{\eta}$	wave height of boundary waves;
θ	slope angle of a channel;
λ	ratio of the heat conductivity of ice to that of water ($= k_s/k_f$);
ν	kinematic viscosity;
ρ	density of water;
ρ_a	air density;
ρ_s	density of ice;
$\tilde{\tau}_{xx}, \tilde{\tau}_{xz}, \tilde{\tau}_{zz}$	components of the stress tensor;
ψ	stream function;
ω	complex angular frequency of a perturbation;
$\tilde{\nabla}, \nabla$	dimensional and nondimensional two-dimensional nabla operators, respectively;
\sim	dimensional version of the corresponding variables;
$\hat{}$	coefficient of Z_1 in the corresponding variable;
$\{ \}_0$	variables in the base state;
$\{ \}_1$	variables in the order of A .

Acknowledgments

The original photographs, some of which are used in this paper and the others were used to measure the wavelength and wave height of steps are available at <http://sites.google.com/site/miwayokokawawebsite/open-data>. This study was supported partly by the Grant for Joint Research Program of the Institute of Low Temperature Science (ILTS), Hokkaido University (proposal 12-59) and Grant-in-Aid for Challenging Exploratory Research (24654165) from JSPS. We offer our thanks to Isaac Smith, John W. Holt, and Wonsuck Kim for their valuable discussion. Hiroki Shimizu, Tadahiro Kitayama, Toru Batani, Shinya Yamamoto, Haruka Kuse, Kazunori Takahashi and the staff of ILTS helped make this research possible. We also thank the editors, Giovanni Coco and Michel Louge, and the three reviewers, Carlo Camporeale, Matthieu Cartigny, and an anonymous reviewer, for their helpful guidance and suggestions.

References

- Alexander, J., J. S. Bridge, R. J. Cheel, and S. F. Leclair (2001), Bedforms and associated sedimentary structures formed under supercritical water flows over aggrading sand beds, *Sedimentology*, *48*, 133–152, doi:10.1046/j.1365-3091.2001.00357.x.
- Ashton, G. D., and J. F. Kennedy (1972), Ripples on underside of ice cover of rivers, *J. Hydraul. Eng. Div.*, *98*, 1603–1624.
- Bregoli, F. (2008), Setting of an experimental flume and first experiments in gravel bed river's morphodynamics (in Italian), Graduate thesis, Eng. Fac. Univ of Florence, Florence, Italy.
- Brooks, P. (2001), Experimental study of erosional cyclic steps, MS thesis, Univ. of Minnesota, Minnesota.
- Camporeale, C. (2015), Hydrodynamically locked morphogenesis in karst and ice flutings, *J. Fluid Mech.*, *778*, 89–119.
- Camporeale, C., and L. Ridolfi (2012), Ice ripple formation at large Reynolds numbers, *J. Fluid Mech.*, *694*, 225–251, doi:10.1017/jfm.2011.540.
- Carey, K. L. (1966), Observed configuration and computed roughness of the underside of river ice, *U.S. Geol. Surv. Prof. Pap.*, *550-B*, US Geol. Surv., St. Croix River, Wisconsin.
- Carey, K. L. (1967), Underside of river ice, *Geol. Surv. Prof. Pap.* 575-C, U.S. Govt. Print. Off., St. Croix River, Wisconsin, Washington.
- Cartigny, M. J. B., D. Ventra, G. Postma, and J. H. van den Berg (2014), Morphodynamics and sedimentary structures of bedforms under supercritical-flow conditions: New insights from flume experiments, *Sedimentology*, *61*, 712–748, doi:10.1111/sed.12076.
- Colombini, M., and A. Stocchino (2008), Finite-amplitude river dunes, *J. Fluid Mech.*, *611*, 283–306, doi:10.1017/S0022112008002814.
- Fahnestock, M. A., T. A. Scambos, C. A. Shuman, R. J. Arthern, D. P. Winebrenner, and R. Kwok (2000), Snow megadune fields on the East Antarctic Plateau: Extreme atmosphere-ice interaction, *Geophys. Res. Lett.*, *27*(22), 3719–3722.
- Frezzotti, M., S. Gandolfi, and S. Urbini (2002), Snow megadunes in Antarctica: Sedimentary structure and genesis, *J. Geophys. Res.*, *107*(D18), 4344, doi:10.1029/2001JD000673.
- Friehe, C. A., and K. F. Schmitt (1976), Parameterization of air-sea interface fluxes of sensible heat and moisture by the bulk aerodynamic formulas, *J. Phys. Oceanogr.*, *6*, 801–809.

- Fuhs, A. E., R. Stolfi, R. Erman, W. Clifford, W. Denner, P. Wang, R. Bourke, and O. Griffin (1980), Experiments involving melting of a large ice block towed in sea water, *Cold Reg. Sci. Technol.*, *1*, 249–264.
- Fukuoka, S., K. Okutsu, and M. Yamasaka (1982), Dynamic and kinematic features of sand waves in upper regime [in Japanese], *Proc. Jpn Soc. Civ. Eng.*, *323*, 77–89.
- Garratt, J. R., and P. Hyson (1975), Vertical fluxes of momentum sensible heat and water vapour during the air mass transformation experiment (AMTEX) 1974, *J. Meteorol. Soc. Jpn.*, *53*(2), 149–160.
- Gilpin, T., R. R. Hirata, and K. C. Cheng (1980), Wave formation and heat transfer at an ice-water interface in the presence of a turbulent flow, *J. Fluid Mech.*, *99*, 619–640.
- Izumi, N., M. Yokokawa, and G. Parker (2012), Cyclic step morphology formed on bedrock [in Japanese with English abstract], *Annu. J. Jpn. Soc. Civ. Eng., Ser. B1*, *68*(4), 1_955–1_960.
- Julien, P. Y., and G. J. Klaassen (1995), Sand-dune geometry of large rivers during floods, *J. Hydraul. Eng.*, *121*(9), 657–663.
- Komori, S., R. Kurose, N. Takagaki, S. Ohtsubo, K. Iwano, K. Handa, and S. Shimada (2011), Sensible and latent heat transfer across the air-water interface in wind-driven turbulence, in *Gas Transfer at Water Surfaces 2010*, edited by S. Komori, W. McGillis, and R. Kurose, pp. 78–89, Kyoto Univ. Press, Kyoto, Japan.
- Kondo, J. (1975), Air-sea bulk transfer coefficients in diabatic conditions, *Boundary Layer Meteorol.*, *9*, 91–112.
- Kostic, S., O. Sequeiros, B. Spinewine, and G. Parker (2010), Cyclic steps: A phenomenon of supercritical shallow flow from the high mountains to the bottom of the ocean, *J. Hydro-environ. Res.*, *3*, 167–172.
- Lajeunesse, E., L. Malverti, P. Lancien, L. Armstrong, F. Metivier, S. Coleman, C. E. Smith, T. Davies, A. Cantelli, and G. Parker (2010), Fluvial and submarine morphodynamics of laminar and near-laminar flows: A synthesis, *Sedimentology*, *57*, 1–26, doi:10.1111/j.1365-3091.2009.01109.x.
- Large, W. G., and S. Pond (1982), Sensible and latent heat flux measurements over the ocean, *J. Phys. Oceanogr.*, *12*, 464–482.
- Núñez-González, F., and J. P. Martín-Vide (2011), Analysis of antidune migration direction, *J. Geophys. Res.*, *116*, F02004, doi:10.1029/2010JF001761.
- Parker, G., and N. Izumi (2000), Purely erosional cyclic and solitary steps created by flow over a cohesive bed, *J. Fluid Mech.*, *419*, 203–238.
- Rajaratnam, N. (1967), Hydraulic jumps, in *Advances in Hydrosience*, vol. 4, edited by V. T. Chow, pp. 197–280, Academic Press, New York.
- Recking, A., V. Bacchi, M. Naaim, and P. Frey (2009), Antidunes on steep slopes, *J. Geophys. Res.*, *114*, F04025, doi:10.1029/2008JF001216.
- van Rijn, L. C. (1984), Sediment transport, Part III: Bed forms and alluvial roughness, *J. Hydraul. Eng.*, *110*(12), 1733–1754.
- Smith, I. B., J. W. Holt, A. Spiga, A. D. Howard, and G. Parker (2013), The spiral troughs of Mars as cyclic steps, *J. Geophys. Res. Planets*, *118*, 1835–1857, doi:10.1002/jgre.20142.
- Smith, I. B., A. Spiga, and J. W. Holt (2014), Aeolian processes as drivers of landform evolution at the South Pole of Mars, *Geomorphology*, *240*, 54–69.
- Smith, S. D. (1980), Wind stress and heat flux over the ocean in gale force winds, *J. Phys. Oceanogr.*, *10*, 709–726.
- Solari, L., and G. Parker (2013), On the morphodynamic modelling of the bottom of ice covers in brackish lakes, *J. Geophys. Res. Earth Surf.*, *118*, 1432–1442, doi:10.1002/jgrf.20115.
- Taki, K., and G. Parker (2005), Transportational cyclic steps created by flow over an erodible bed. Part 1. Experiments, *J. Hydraul. Res.*, *43*(5), 488–501.
- Vesipa, R., C. Camporeale, and L. Ridolfi (2015), Thin-film-induced morphological instabilities over calcite surfaces, *Proc. R. Soc. A*, *471*(2176), 20150031.
- Yokokawa, M., K. Okuno, A. Nakamura, T. Muto, Y. Miyata, and H. Naruse (2009), Aggradational cyclic steps: Sedimentary structures found in flume experiments, paper presented at 33rd IAHR Congress, pp. 5547–5554, Vancouver, Aug.
- Yokokawa, M., Y. Takahashi, H. Yamamura, Y. Kishima, G. Parker, and N. Izumi (2011), Phase diagram for antidunes and cyclic steps based on suspension index, non-dimensional Chezy resistance coefficient and Froude number, in *Proceedings of the 7th IAHR Symposium on River, Coastal and Estuarine Morphodynamics (RCEM 2011)*, Sept., edited by X. Shao et al., pp. 1789–1794, Tsinghua Univ., Beijing, China.